MASTER

Time-of-Flight electron energy loss spectroscopy using a TM010 cavity for longitudinal phase space manipulation

Toonen, Wiebe F.

Award date:
2017

Time-of-Flight Electron Energy Loss Spectroscopy using a TM_{010} cavity for longitudinal phase space manipulation

W.F. Toonen

May 2017

A thesis for the degree of Master of Science (MSc.)

Master of Applied Physics
Eindhoven University of Technology
Department of Applied Physics
Coherence and Quantum Technology (CQT)
Supervisors: dr. ir. P.H.A. Mutsaers,
W. Verhoeven, MSc.

CQT 2017-08

Abstract

Electron Energy Loss Spectroscopy (EELS) is a technique based on the kinetic energy loss of electrons after interacting with a sample. The energy loss distribution is characteristic to the sample, allowing for material analysis. These different electron energies are usually measured with an expensive magnetic prism spectrometer. Previous work has shown that the energies can also be separated by a microwave TM_{110} cavity based on time-of-flight. These cavities are metallic resonators containing time-dependent electromagnetic fields. Separating the electron energies in this way requires electron pulses rather than a continuous beam, and they are usually made by shining a pulsed laser onto a cathode. In our setup, the creation of pulses will be done by focusing a continuous electron beam from a 30 kV scanning electron microscope in the center of another TM_{110} cavity. In combination with a slit, electron pulses with a temporal pulse length of 3 ± 1 ps can be generated. This method has been dubbed Time-of-flight Electron Energy Loss Spectroscopy (ToF-EELS). With recent measurements using this method an EELS spectrum was acquired with a full width at half maximum (FWHM) energy spread of 10.8 ± 0.2 eV, which is still much higher than the ~0.1 eV obtained in state-of-the-art electron microscopes using monochromators.

In this thesis a way of improving the energy resolution of the ToF-EELS method is presented. This is done by inserting a TM_{010} cavity into the current setup. Along the z-axis of the TM_{010} or transverse magnetic monopole mode is a time-dependent electric field that oscillates parallel to the z-axis. Passing an electron bunch through this cavity around the zero phase will slow down the front while accelerating the back, causing the bunch to be compressed. This being equivalent to longitudinal lensing, there will be a point where electrons with initially identical energies end up on identical longitudinal positions. With the energies now separated longitudinally in space, a TM_{110} cavity can be used to separate them transversally onto the detector.

In order to accommodate the TM_{010} compression cavity, adjustments to the ToF-EELS setup were made. With the new experimental setup waist scans were performed by varying the power in the TM_{010} cavity, characterising the bunch compression. At optimal compression, a spot size an order of magnitude higher than the $31.3\,\mu$m from simulations was found. Further inspection revealed that the electron spot was distorted. Suspecting electromagnetic interference, surrounding devices were investigated using an AC magnetic field meter and subsequently moved or removed. Although this did increase the beam quality, the distortion persisted. By employing a beam blanker at 50 Hz synchronized to the power grid, it was possible to isolate one spot from the distortion, allowing for proper measurements to be performed.

New waist scans were performed and a minimum spot size of $28.5 \pm 0.2\,\mu$m was found. A carbon film covered with a polycrystalline gold layer was inserted and an electron energy loss spectrum was taken. From this spectrum the FWHM energy resolution was calculated to be 2.3 ± 0.1 eV, proving that adding a TM_{010} cavity greatly improves the energy resolution of the ToF-EELS method.

Contents

Chapter 1

Introduction

1.1 Electron Microscopy: A brief history

Throughout history, lenses and microscopes have continuously been improved upon. From first century Romans, who found objects appeared larger when viewed through glass, to Antoni van Leeuwenhoek's superior lenses, allowing him to look at bacteria. It was not until 1873 when Ernst Abbe found the limitations of optical microscopy; The *Abbe diffraction limit* restricts optical systems from distinguishing between objects separated by less than approximately half the wavelength of the light used. To increase the spatial resolution below this ~200 nm, light with shorter wavelengths, such as UV or X-Ray, could be used.
A different solution became possible after the *De Broglie hypothesis* was formulated in 1924 and confirmed for electrons three years later: electrons also behave as waves. The field of electron microscopy was born and in 1933 an electron microscope exceeding the resolution attainable by optical microscopes was built[1]. Since then, electron microscopes have continued to improve and have contributed to many fields, such as the life sciences and the physical sciences.

A crucial aspect of an electron microscope is the obtainable resolution. Taking for example a 30 kV scanning electron microscope (SEM), the De Broglie wavelength λ of the electrons is 7 pm, which is much smaller than the wavelength of visible light ($\lambda \approx 550$nm). However, the resolution of current electron microscopes is not limited by the Abbe diffraction limit, but by aberrations. The Scherzer Theorem states that the aberration coefficient in rotationally symmetric space-charge-free electron lenses is always positive[2]. This means that the aberrations cannot be compensated for with lenses with a negative aberration coefficient, limiting the resolution of electron microscopes to 50–100 times the electron wavelength.
In order to bypass this limitation much work has been done on aberration correction[3]. Many different multipole setups were designed to this end, but until the 1990s they all failed. If you take for example a quadrupole-octopole system, the setup becomes impossible to align and adjust, as such a system has many different parts that all need to be positioned and operated with a high accuracy. Doing this near the optical axis is difficult enough, but in a transmission electron microscope (TEM) corrections need to be done over the entire region to be imaged. In a system where the octopoles need to correct both small and large aberrations simultaneously due to the objective lens and quadrupoles, small misalignments will lead to huge aberrations.
As operating a quadrupole-octopole system was too difficult in a TEM, a setup with this correcting system was described in 1990 for a low-voltage SEM[4]. The 1990s also experienced a rapid increase in computing power, allowing for fast computer control to make adjustments.

These two combined delivered the first successful result in aberration correction[5]. Improvements and successes in other systems followed quickly[6][7][8] and in the subsequent years sub-ångström resolution was achieved[9].

Not only the spatial resolution but also the temporal resolution has been improved upon over the past years. First attempts involved recording TEM images on photographic film with exposure times of a few seconds, but with the invention of the charge-coupled device (CCD) cameras in 1969 and the general improvement of computers it became possible to achieve millisecond exposure times and interframe times[10]. Dynamic phenomena on these characteristic time scales, for example motions in deforming metals, could now be studied. Improvement continued and in 1983 microsecond temporal resolution was achieved by using a combination of a thermal emission source and streak-plates, achieving sub-microsecond electron pulses[11]. Some structural changes in biology could now be measured, yet many processes, such as molecular vibrations, occur at much smaller time scales ($<10^{-12}$ s). In order to achieve sub-picosecond pulses a femtosecond laser extracts an electron beam from a photocathode in ultrafast packets with as few as one electron per pulse. These packets are then accelerated to 30–200 kV and are used to image for example expansion and contraction in a crystal[12]. An advantage of such a system is that the laser is automatically synchronized to the electron pulses. This can be used in for example pump-probe experiments.

The field of Ultrafast Electron Microscopy (UEM) utilizes many different techniques such as photon induced near-field electron microscopy (PINEM), scanning transmission electron microsopy (STEM) and electron energy loss spectroscopy (EELS)[13]. Here at the group of Coherence and Quantum Technology (CQT) at the Eindhoven University of Technology (TU/e), research is being done on using microwave cavities for electron microscopy. Since microwave cavities can contain a time-dependent field, Scherzer's theorem does not apply and both spherical and chromatic aberrations can be corrected for, opening up possibilities for use in a TEM. This thesis however will focus on using microwave cavities to generate, compress and achieve electron energy separation of electron pulses in order to perform EELS. The next section will provide a brief description about EELS itself, while Section 2.4 will discuss the physics of EELS. Section 1.3 will give an overview on how microwave cavities are used to perform EELS.

1.2 An introduction to EELS

In electron energy loss spectroscopy an electron beam is pointed at a specimen. The electrons will either pass through the sample without interacting, or they will interact through the Coulomb force with the atoms in the sample. In this interaction an incident electron can lose some of its energy to the specimen. After passing through the sample, the electron beam is directed towards a spectrometer capable of separating the electrons according to their kinetic energy. An example of such a spectrometer is a magnetic prism spectrometer: an electromagnet with a uniform magnetic field. Due to the Lorentz force, the incoming electrons travel in a circular orbit with radius of curvature $R = (\gamma m_e v/eB)$ with γ the Lorentz factor, m_e the electron rest mass, e the elementary charge, B the magnetic field strength and v the electron velocity. With a constant magnetic field, R is only dependent on the velocity of the electrons, causing electrons with different kinetic energies to hit a different part of an electron detector, achieving energy separation.

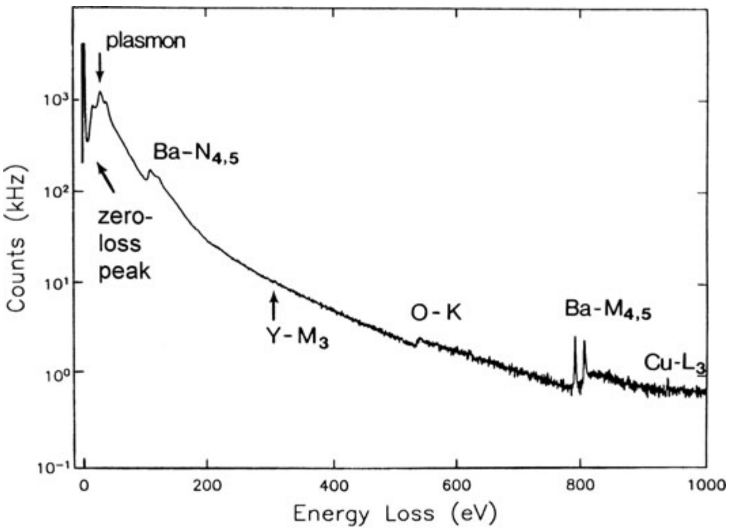

Figure 1.1: Electron energy-loss spectrum of a high-temperature superconductor ($YBa_2Cu_3O_7$) with the electron intensity on a logarithmic scale, showing zero-loss and plasmon peaks and ionization edges arising from each element. *From* [14].

Doing an EELS measurement results in a typical electron energy loss spectrum as shown in Fig. 1.1, displaying the number of electrons as a function of energy loss. Such a spectrum contain several features of interest: the zero-loss peak (ZLP), the plasmon peak and ionization edges. These will be discussed in more detail in Section 2.4. The features in an electron energy-loss spectrum are characteristic to the elements present in the specimen, which allow for the identification of elements.
With EELS it is also possible to distinguish between different structures of the same element, for example diamond, graphite and amorphous carbon. All three are allotropes of carbon, but since their plasmon peaks occur at different energies they can still be distinguished. Not only is EELS used to both qualitatively and quantitatively identify elements, the sharp rises in the spectrum occur at the binding energy of an atomic shell and allow for research into bandgap energies.

While there are many applications of EELS, some of those require high resolutions. An example is the detection of surface plasmon resonances which typically lie below 5 eV. Due to the relatively high intensity of the zero-loss peak and the small intrinsic width of these features, an energy resolution of approximately 0.1eV is required[15]. Since the aim is to measure differences in electron energy, the initial energy spread of the electron beam should be as low as possible. Different types of electron emitters exists and one of them is a thermionic emitter, where electrons flow from the surface due to their thermal energy overcoming the work function of the cathode. This effect can be further enhanced by negatively biassing the emitter, causing the local surface barrier to be lowered. This is known as the Schottky effect. Thermionic emitters have a typical energy spread between 1 and 3 electronvolt (eV). Another type of electron emitter is the field emission gun (FEG). Here a sharply pointed filament is held at negative potential in the order of kilovolts relative to a nearby cathode. The high potential gradient then lowers the work function of the material, allowing electrons to tunnel out of the material. With this technique even lower energy spreads were achieved, reaching 0.25 eV in a cold FEG. Combining these emitters with a monochromator reduces the energy spread even further, going down to or even below 0.1 eV, at the cost of beam current[16].

1.3 The method of Time-of-Flight EELS

A vital part of EELS is the separation of electrons with different energies. Instead of using an expensive magnetic prism spectrometer, this will be done with a TM_{110} microwave cavity, which will be discussed in Section 2.2. When an electron bunch passes through a specimen, the specimen will impose an energy distribution onto the electrons. If the bunch is then allowed to drift a certain distance, the electrons with higher energies will cross this distance in less time. This means that the energy distribution has been changed into a temporal distribution. Inserting a cavity with a time-dependent magnetic field will cause the electrons to be subjected to a Lorentz force. However, since the magnetic field is time-dependent the Lorentz force will vary with the arrival time of the electrons. This means the electrons are streaked transversally according to their time of flight. Hence the method is called Time-of-Flight EELS (ToF-EELS). Placing an electron detector behind this *streaking cavity* will result in a spatial distribution of electrons that corresponds to the original energy distribution caused by the sample, achieving energy separation.

The method of ToF-EELS does require electron pulses. As mentioned before, these are usually created using a femtosecond laser. This project instead uses a TM_{110} cavity to generate picosecond electron pulses, eliminating the need of a complicated laser setup. The way this is done is by passing a continuous electron beam through the center of the cavity. The time-dependent magnetic field will again deflect the electrons, creating 'waves' of electrons. Placing a slit perpendicular to the direction of deflection behind the cavity will only allow certain parts of this wave to pass through, creating electron bunches. This is called *chopping*. An overview of the ToF-EELS method is shown in Fig. 1.2, and since it uses two cavities it will be referred to as the two-cavity setup.

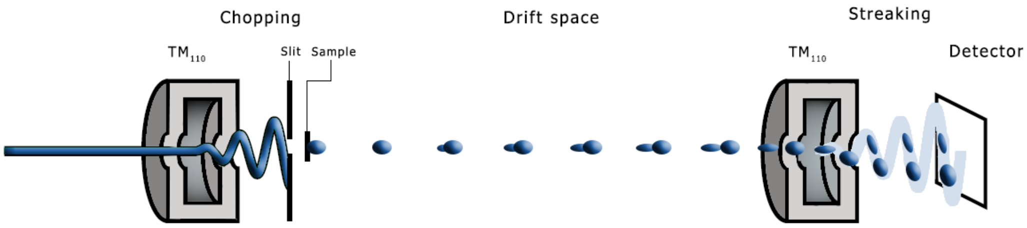

Figure 1.2: The working principle of ToF-EELS. The chopping cavity and the slit chop the beam. The chopped beam then passes through a sample, which creates energy differences within a bunch. The drift space transforms these energy differences into temporal differences. The final cavity then streaks the bunches onto a position on the detector based on their arrival time.

1.4 Scope of this thesis

Earlier experiments have given proof-of-principle for the ToF-EELS method, achieving a FWHM temporal resolution of approximately 2.9 ps and a FWHM energy resolution of approximately 13 eV as measured by the width of the ZLP[17]. This is however a rather poor resolution compared to a commercial spectrometer. The reason for this is that the resolution in the detection of the flight time depends on the initial pulse length. As different energies need to become separated temporally, shorter pulses are required to make them distinguishable.

This thesis will attempt to improve the energy resolution to the single eV range, as well as to provide an outlook on how sub-eV resolutions can be obtained. This will be done by inserting a TM_{010} cavity into the drift space, creating a three-cavity setup (see Fig. 1.3). The TM_{010} cavity is able to compress the electron bunches, decreasing the pulse length. As will be shown, this can be done while maintaining the temporal separation due to the different velocities of electrons behind the compression cavity. This greatly increases the flight-time resolution and thus the energy resolution. How this works will be discussed in more detail in Section 2.1.2. Section 2.2 and Section 2.3 will give an in-depth description of respectively the microwave cavities and their effects on an electron beam, while Section 2.4 will go into the physics of EELS. In Chapter 3 the current setup will be discussed, as well as the changes made to it to accommodate the extra cavity. In order to confirm the previously found energy resolution an electron energy loss spectrum is taken with the two-cavity ToF-EELS method and its results will be discussed in Chapter 4. The experiments performed with the three-cavity setup will investigate the performance of the TM_{010} cavity as well as its effects on an EELS measurement and can be found in Chapter 5. Finally in Chapter 6 a conclusion and outlook will be presented as well as recommendations for further improvements.

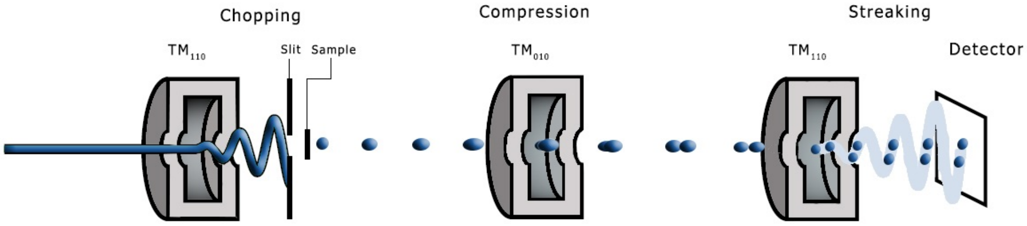

Figure 1.3: The working principle of three-cavity ToF-EELS. The chopping cavity and the slit chop the beam. The chopped beam then passes through a sample, which creates energy differences within a bunch. The TM_{010} cavity compresses the electron bunches, which separates the different energies longitudinally. The final cavity then streaks the different energies to different positions on the detector.

Chapter 2

Theory

As mentioned in the introduction, the new method of ToF-EELS uses two types of microwave cavities in order to manipulate electrons: one containing the TM_{110} mode and one containing the TM_{010} mode. This chapter will explain in depth the theory involved with the ToF-EELS method, as well as cavities and their effects on an electron beam. In Section 2.4 a detailed description of the physical processes involved in electron scattering and their relevancy to EELS will be given. Finally, one of the measurements that will be done with the three-cavity setup is a waist scan, which Section 2.3.4 will give a description of.

2.1 ToF-EELS

2.1.1 ToF-EELS without a TM_{010} cavity

As mentioned in the introduction, our group has been developing a new method of doing EELS using microwave cavities. This method, called Time-of-Flight EELS, uses TM_{110} microwave cavities to achieve both electron pulse generation and separation of electron energies based on their time-of-flight. While earlier experiments have given proof-of-principle for this method, the achieved energy resolution was only 13 eV. In order to find the limitation that causes this poor resolution, a description of the longitudinal phase space of an electron bunch is necessary.

In general, a phase space is a space which represents all the possible states of a system. Defining the propagation of direction of the electron beam along the positive z-axis, an example for the transverse x-direction is the phase space consisting of all x-positions and all particle angles $x' = \mathrm{d}x/\mathrm{d}z$. For the longitudinal phase space, one dimension consists of all the possible z-positions relative to the center of mass of the bunch, but since there is no such thing as a longitudinal angle an equivalent will be used for the other dimension:

$$z' = \frac{v_{z,i} - v_z}{v_z}, \tag{2.1}$$

with z' the longitudinal divergence, $v_{z,i}$ the velocity of the corresponding electron and v_z the average velocity. Although the longitudinal phase space is defined slightly different from the transversal phase space, all the same manipulations such as a drift or focusing work in a similar manner.

On the left side of Fig. 2.1 a the longitudinal phase space of a bunch is shown schematically directly after it has interacted with a sample. The sample has imposed an energy distribution on the bunch, which is represented by the different relative velocities. In the drift space the electrons will propagate according to their respective velocities, causing the higher velocities

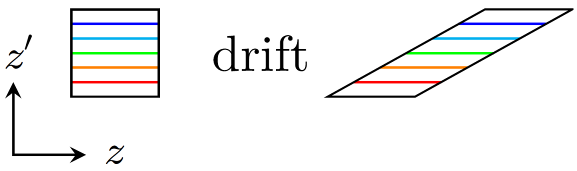

Figure 2.1: The longitudinal phase space of an electron bunch. The sample creates a velocity distribution as indicated by the colors. The drift space causes separation based on these velocities, which corresponds to the shearing of the bunch.

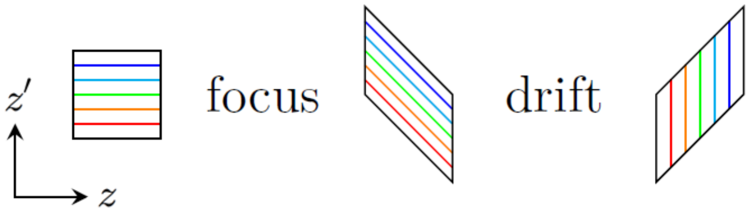

Figure 2.2: The longitudinal phase space of an electron bunch. Interaction with the sample causes electrons to lose some amount of energy as indicated by the colors. The compression cavity focuses the bunch, which corresponds to the vertical shear. After drifting a certain distance the electrons will line up in the longitudinal direction according to their energy loss.

to get ahead while the lower velocities lag behind, separating the electron energies. This is represented by the sheared bunch on the right side of Fig. 2.1. The streaking cavity will then separate the electrons based on their arrival time, which corresponds to their position in this sheared bunch. However, looking at a single position it becomes apparent that there is still much overlap between different velocities and thus energies if the initial pulse length is too large or the drift space too small. It is this overlap that limit the energy resolution of the current ToF-EELS method.

2.1.2 ToF-EELS with a TM_{010} cavity

In order to improve the energy resolution of the ToF-EELS method, the overlap between the different energies in an electron bunch should be minimized. To this end a TM_{010} microwave cavity will be used. Along the z-axis of such a cavity there is a time-dependent electric field that oscillates parallel to the z-axis[18]. By properly setting the phase of this electric field the front of the electron bunch can be slowed down while the rear of the bunch is accelerated, initiating a bunch compression[19][20]. The TM_{010} cavity is therefore called the *compression cavity*. This compression can also be regarded as longitudinal lensing, which will be expanded upon in Section 2.3.2.

A certain drift length after the TM_{010} cavity the electron bunch will be compressed to a fraction of its original length, depending on the beam parameters and the focusing power of the compression cavity. At the point of optimal compression, different energy losses are then well separated. The phase space representation of this process is shown in Fig. 2.2. Starting again with an electron bunch with a certain energy distribution, the compression cavity will decrease the velocity of the front of the bunch while increasing the velocity at the rear. This is represented by a vertical shear. In the drift space the electrons will again propagate according to their respective velocities, corresponding to a horizontal shear.

This will now cause all originally identical velocities to align at identical positions without overlap, independent of pulse length or drift distance.

The velocity distribution directly behind the sample is however not solely dependent on the energy losses created by the sample, but also by the energy spread the electron bunches have before they interact with the sample. A way to decrease this energy spread is to use another TM_{010} cavity in front of sample to stretch the electron pulses. This will be discussed in more detail in Section 6.2.1.

2.2 Microwave cavities

2.2.1 Microwave cavities in general

A cavity is a resonator that confines electromagnetic fields. For laser systems this is called an optical cavity, as it confines light from the visible spectrum using an arrangement of mirrors. Cavities designed for microwaves however are formed by an (almost) completely closed off metal structure. The cavity walls cause microwaves to reflect, creating a standing wave at the resonant frequencies of the cavity. These resonant frequencies are determined by several aspects, such as cavity size, geometry and filling. Microwave cavities are used in numerous applications, ranging from satellite communications to microwave ovens.

2.2.2 The $\mathbf{TM_{110}}$ and $\mathbf{TM_{010}}$ mode

The electromagnetic field components in a microwave cavity are derived by taking Maxwell's equations and applying the appropriate boundary conditions. This has been done for many general cases and as such no derivation will be given here. The general theory on this subject can be found here: [21].

The field modes of interest in this thesis are the TM_{110} and TM_{010} mode, which are visualised in Fig. 2.3 and Fig. 2.4 for a circular configuration. These modes are called transverse magnetic ($\mathrm{TM}_{\mathrm{lmn}}$) because the corresponding field in the propagation direction is zero, i.e. $B_z = 0$. The modes are further characterized by the three integers l, m and n and describe the eigenvalues of the wave vector k of the fields. For circular configurations these can also be viewed as the amount of full-wave patterns in the θ-, r- and z-direction.

For the TM_{010} mode, assuming perfectly conducting walls as described by $E_z\,(r \to R) = 0$, the field components in cylindrical coordinates are given by [22]:

$$E_z(r,t) = E_0 J_0\,(kr)\cos(\omega t), \tag{2.2}$$

$$B_\theta(r,t) = \sqrt{\epsilon\mu}E_0 J_1\,(kr)\sin(\omega t). \tag{2.3}$$

Here E_0 is the electric field amplitude, J_n is the n^{th} order Bessel function of the first kind, $\epsilon = \epsilon_r\epsilon_0$ the permittivity and $\mu = \mu_r\mu_0$ the permeability of the material inside the cavity, $k = \omega\sqrt{\epsilon_r}/c$ the wave number and $\omega = 2\pi f$ the angular frequency with f the frequency of the resonant mode. A cavity containing a vacuum has $\epsilon_r = \mu_r = 1$, so $\sqrt{\epsilon\mu} = \sqrt{\epsilon_0\mu_0} \equiv 1/c$ with c the speed of light in vacuum. From this follows that an electron travelling through the center of the cavity ($r \approx 0$) will either be accelerated or decelerated by the longitudinal electric field, while it is approximately unaffected by the magnetic field.

For the TM_{110} mode the relevant field components are given by

$$E_z(r,\theta,t) = \frac{2B_0}{\sqrt{\epsilon\mu}} J_1\left(kr\right)\cos(\theta)\sin(\omega t), \tag{2.4}$$

$$B_r(r,\theta,t) = \frac{1}{r\omega}\frac{2B_0}{\sqrt{\epsilon\mu}} J_1\left(kr\right)\sin(\theta)\cos(\omega t), \tag{2.5}$$

$$B_\theta(r,\theta,t) = \frac{1}{\omega}\frac{2B_0}{\sqrt{\epsilon\mu}}\frac{\partial}{\partial r} J_1\left(kr\right)\cos(\theta)\cos(\omega t), \tag{2.6}$$

where B_0 is the magnetic field amplitude defined such that $B_y(r=0,t=0)=B_0$. From these fields one can see that electrons passing through the center will not be affected by the electric field, while they will experience a Lorentz force $\vec{\mathbf{F}} = q\cdot\left(\vec{\mathbf{v}}\times\vec{\mathbf{B}}\right)$ due to the transverse magnetic field.

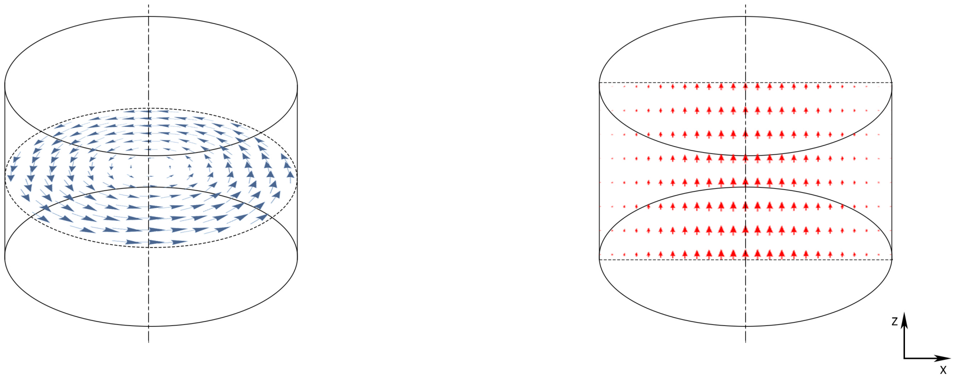

(a) The B-field

(b) The E-field

Figure 2.3: The electric and magnetic field modes of the TM_{010} pillbox cavity with height d and radius R. The electron path is indicated by the dash-dotted line and runs along the z-axis.

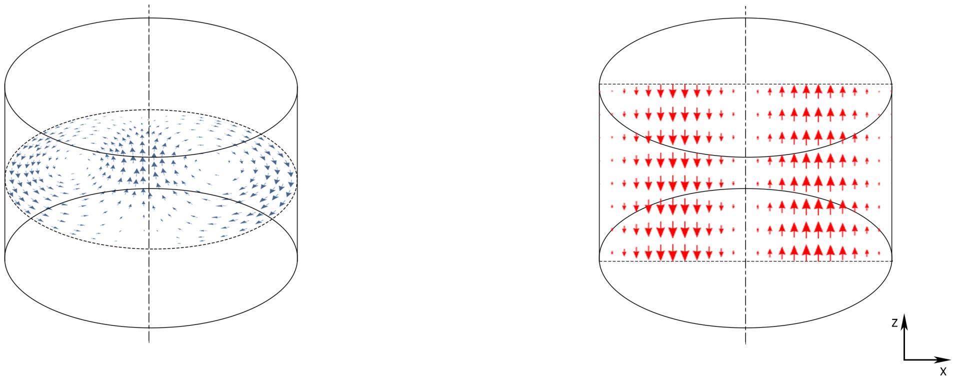

(a) The B-field

(b) The E-field

Figure 2.4: The electric and magnetic field modes of the TM_{110} pillbox cavity with height d and radius R. The electron path is indicated by the dash-dotted line and runs along the z-axis.

The resonant frequency is an important property of a cavity and for a $\mathrm{TM_{lmn}}$ mode it is given by[23]

$$\omega_{lmn} = \frac{1}{\sqrt{\epsilon\mu}}\sqrt{\frac{x_{lm}^2}{R^2} + \frac{n^2\pi^2}{d^2}}, \tag{2.7}$$

with x_{lm} the n^{th} root of $J_l(x) = 0$. For the $\mathrm{TM_{010}}$ mode this means that the resonant frequency is

$$\omega_0 = \frac{x_{01}}{R\sqrt{\epsilon\mu}}, \tag{2.8}$$

where $x_{01} \approx 2.405$. All cavities used in this project are designed to operate at a frequency of approximately 3 GHz. This frequency is chosen because in this frequency range many properties of materials are well-documented, appropriate equipment is widely available and it is the 40^{th} harmonic of 75 MHz which allows for synchronization with a Ti:Sapph laser oscillator. With a frequency of 3 GHz it follows from Eq. 2.8 that a $\mathrm{TM_{010}}$ pillbox cavity containing a vacuum must have a radius $R = 38.3\,\text{mm}$. A similar calculation can be done for the $\mathrm{TM_{110}}$ mode, where $x_{11} \approx 3.832$, which leads to a cavity radius of $R = 60.9$ mm.

As for the height d of the cavity, it is apparent both from the field components and Eq. 2.7 with $n = 0$ for both modes of interest that the resonant frequency does not depend on it. The height of the cavity does determine the interaction time the electrons have with the electromagnetic fields and thus the effect the cavity has on the electron beam. In order to maximize the total force enacted on the electrons, a pillbox configuration must have a height with which the electrons will interact with half a period of the field. The distance travelled by 30 keV electrons in half a period of a 3 GHz cavity is given by $v_z/2f \approx 16.4$ mm. In practice, the length of the interaction region in the $\mathrm{TM_{110}}$ cavities is 16.7 mm. As will be discussed in the next section, the compression cavity has a different geometry that increases the electric field strength in the interaction region by decreasing the length of the interaction region, leading to a smaller height of 6 mm.

2.2.3 Cavity design overview

Throughout earlier projects much time has been invested in order to increase the power efficiency of these cavities. One way of doing this is by increasing the unloaded Q-factor Q_0. Not only does a higher Q-factor decrease the required input power, it also means the cavity will have a smaller bandwidth. In general a higher Q-factor can be achieved by either increasing the stored energy U_{strd} or by decreasing the power lost P_{T} through dissipation:

$$Q_L = \omega\frac{U_{\text{strd}}}{P_{\text{T}}}, \tag{2.9}$$

with Q_L the loaded Q-factor and the total power loss $P_{\text{T}} = P_{\text{cav}} + P_{\text{ext}}$, the power lost through respectively the cavity walls and holes in the cavity geometry. The unloaded quality factor Q_0 and the external quality factor Q_{ext} follow a similar relation as Eq. 2.9, with

$$\frac{1}{Q_L} = \frac{1}{Q_0} + \frac{1}{Q_{\text{ext}}}. \tag{2.10}$$

Where in the calculations of the field components of both modes perfectly conducting walls were assumed, in reality they have a finite conductivity leading to induced currents and thus losses due to Ohmic heating. One way of reducing these losses is by minimizing the magnetic field amplitude near the cavity walls. Doing this with a geometry where the field is also concentrated around the electron interaction region to optimize the stored energy results in a sharp increase of Q_0; whereas the simple 3 GHz TM_{010} pillbox cavity has a quality factor of $Q_0 = 4.3 \cdot 10^3$, the optimized geometry has a Q-factor of $8.3 \cdot 10^3$.

For the chopping and streaking cavities a miniaturized design was created by using a dielectric material with $\epsilon_r > 1$ inside the cavity. From Eq. 2.7 it follows that the resonant frequency of the cavity will then drop by a factor $\sqrt{\epsilon}$. Due to practical reasons, the current design in not completely filled with dielectric material[17], meaning the net ϵ_r of the cavity is a bit lower than that of the dielectric material. The drop in resonant frequency can be explained by the dielectric material impeding the propagation of the electromagnetic wave. In order to keep $f = 3$ GHz the cavity radius must decrease according to Eq. 2.7, leading to $R = 11.9$ mm.
The dielectric material however will not be a perfect electrical insulator. As such, conduction currents will be induced, leading to power losses. This dissipation of energy is also called *dielectric loss* and is often described with the loss tangent $\tan\delta$. Summarized this means that the dielectric material used should have both a high ϵ_r and a low $\tan\delta$. Luckily these types of materials are readily available and a zirconium titanate ceramic with $\epsilon_r \approx 37$ and $\tan\delta = 2 \cdot 10^{-4}$ in the frequency range of 0.8 to 18 GHz was used (specifications only measured at 10 GHz).
Aside from the geometry and filling, there are several more ways to tune the resonant frequency of the cavity. One of these is the temperature. Since heat causes materials, and by extension holes in materials, to expand, the size and thus the resonant frequency of a cavity will be slightly different for different temperatures. As energy is constantly being dissipated as heat, it is important to keep the cavity temperature constant at a desired value. As such each cavity has a temperature stabilization system using a heating element and either water or air cooling.
For the compression cavity the only material present is copper, which has a thermal expansion coefficient of $\kappa_T = \frac{1}{R}\frac{dR}{dT} = 16.5 \cdot 10^{-6}\,\mathrm{K}^{-1}$ [24]. The change in frequency can then be calculated from Eq. 2.8:

$$\frac{\partial f}{\partial T} = \frac{1}{2\pi}\frac{\partial \omega_0}{\partial T} = \frac{-x_{01}}{2\pi\sqrt{\epsilon\mu}}\frac{1}{R^2}\frac{dR}{dT} = -f_0\kappa_T, \tag{2.11}$$

leading to a frequency shift of $\partial f/\partial T = -49.5$ kHz/K at 3 GHz.
For the TM_{110} cavities there are two other means of tuning the frequency besides the temperature. The first is by inserting a metallic stub into the cavity, which decreases the effective size and thus increases the resonant frequency. The second method is by applying stress on the dielectric material. As the dielectric is essentially clamped between the bottom of the cavity and a screw cap, tightening the screw cap further will increase the stress on the dielectric material, causing the ϵ_r of the material to drop, which in turn decreases the resonant frequency.

The thermal behaviour of the TM_{110} cavities is a bit more difficult to describe. The first complication is the fact that ϵ_r is also temperature dependent, which changes the partial derivative of Eq. 2.7 and requires a factor $\partial\epsilon_r/\partial T$ to be known around 3 GHz for the relevant temperature range. The second complication is that the thermal expansion coefficient of the dielectric is different from the copper. Different expansion rates will cause the stress on the dielectric to vary with temperature, again changing the resonant frequency. Thirdly, while the copper of the cavity is thermalized to ~313 K, resent measurements have shown that the dielectric material can reach temperatures up to ~800 K for an input power of 10 W[25]. There is also very little known about the heat exchange between the copper shell and the dielectric material, such as through thermal contact conductance. This all makes the thermal behaviour of the TM_{110} cavities complicated and largely unexplored.

2.2.4 Power coupling

In order to actually excite the field mode in a cavity, power has to be transferred into it. The electric field strength scales with the square root of the energy stored in the cavity, which in turn is linear with the power absorbed by the cavity[23]. It is therefore required to have maximum power transfer for optimal performance. From the maximum power transfer theorem it is known that, since the power generator has a finite internal resistance, the maximum absolute power is transferred when the efficiency is at 50%. This means that half the generated power will go into the cavity, while half is deposited into the external load. From this a coupling coefficient is defined as

$$\beta \equiv \frac{P_{\text{ext}}}{P_{\text{cav}}} = \frac{Q_0}{Q_E}, \tag{2.12}$$

where $\beta = 1$ is called *critical coupling.* From network theory and this coupling coefficient, a voltage reflection coefficient as seen by the power generator is given by

$$\Gamma|_{f=f_{\text{res}}} = \frac{\beta - 1}{\beta + 1}. \tag{2.13}$$

From this it also follows that for $\beta = 1$, nothing is reflected and maximum power transfer is achieved.

In the compression cavity the electromagnetic fields are induced through the use of a loop antenna, which is often used in frequencies around 3 GHz. This loop antenna has a magnetic dipole moment and couples to the magnetic field through this loop through an inner product. As such, rotating the loop antenna changes the effective area of the loop and therefore changes the amount of coupling to the magnetic field, allowing for maximum power transfer.
For the miniaturized TM_{110} cavities the small dimensions required of the antenna caused some practical difficulties. This is why there was opted for a linear antenna. A linear antenna does not have a magnetic moment, but a dipole moment. This dipole moment then couples to the electric field, also through an inner product. As the length of the antenna changes the magnitude of the dipole moment, this can be used to change the amount of coupling in order to achieve maximum power transfer.

2.3 Electron beam dynamics

2.3.1 Chopping and streaking cavity

With the modes of the two types of cavities known, this section will look into their effects on an electron beam. For all the cavities the electrons will remain near the z-axis. This means that for the TM_{110} cavities, only the transversal magnetic field is of interest. This magnetic field can be approximated by using $\frac{1}{r}J_1(kr) \approx \frac{\partial}{\partial r}J_1(kr) \approx \frac{k}{2}$ for $r \ll R$. Applying this to Eq. 2.5 and Eq. 2.6 and transforming them to Cartesian coordinates results in

$$B_x = 0, \tag{2.14}$$

$$B_y = B_0 \sin(\omega t + \phi), \tag{2.15}$$

with an added phase ϕ to represent the phase of the magnetic field at $t = 0$. With this it is clear that due to the Lorentz force the electrons are deflected in the x-direction. In order to maximize this deflection, the time the electrons take to pass through the cavity should equal half the period of the magnetic field:

$$d = v_z \frac{\pi}{\omega}, \tag{2.16}$$

with v_z the average longitudinal speed of the electrons. With this the electron trajectories can be calculated. Taking an electron with longitudinal velocity v_z and divergence $x_i' = v_{x,i}/v_z$ with $v_{x,i} \ll v_z$, it enters the cavity at a transversal position x_i at a time $t = t_i = -\pi/(2\omega)$ and exits the cavity at $t = t_f = -t_i$. The force experienced by the electron while it is inside the cavity is then given by

$$\vec{\mathbf{F}}(\phi, t) = q \cdot \left(\vec{\mathbf{v}} \times \vec{\mathbf{B}}\right) = -e v_z B_0 \sin(\omega t + \phi)\hat{\mathbf{x}}, \tag{2.17}$$

with e the elementary charge. Integrating this equation yields the transverse electron velocity

$$v_x(\phi, t) = \frac{1}{m_e} \int_{t_i}^{t} \vec{\mathbf{F}} \, \mathrm{d}t + v_z x_i' = \frac{e B_0 v_z}{m_e \omega} \left(\cos\left(\omega t + \phi\right) - \cos\left(\omega t_i + \phi\right)\right) + v_z x_i', \tag{2.18}$$

where m_e is the electron mass. Integrating once more results in the transverse position

$$\begin{aligned} x(\phi, t) &= \int_{t_i}^{t} v_x \, \mathrm{d}t + x_i \\ &= \frac{e B_0 v_z}{m_e \omega^2} \left(\sin(\omega t + \phi) - \sin(\omega t_i + \phi) - \omega \cos(\omega t_i + \phi)\,(t - t_i)\right) + v_z x_i' \,(t - t_i) + x_i. \end{aligned} \tag{2.19}$$

Fig. 2.5 shows the electron trajectories with $x_i' = x_i = 0$ for several phases. From Eq. 2.18 the transverse velocity at $t = t_f$ can be obtained. Assuming $x_i' = 0$ yields

$$v_{x,f} = -\frac{2 e B_0 v_z}{m_e \omega} \sin(\phi) \tag{2.20}$$

which can then be converted into a sweep angle

$$\alpha(\phi) = \frac{v_{x,f}}{v_z} = -\frac{2 e B_0}{m_e \omega} \sin(\phi) \tag{2.21}$$

under which the electrons exit the cavity. Since electrons arriving at the cavity at different times experience a different phase, a continuous beam traversing a TM_{110} cavity will be deflected back and forth periodically. This can be used to create pulses by placing an aperture with a hole size s at a distance l centered around the z-axis. Only those electrons whose sweep angle is smaller than the angle $s/2l$ subtended by the aperture can pass through. Again assuming small angles, this leads to

$$-\frac{s m_e \omega}{4 l e B_0} < \phi < \frac{s m_e \omega}{4 l e B_0}. \tag{2.22}$$

This means that only a small part of the electrons pass through, creating a pulse train of electron bunches (see Fig. 2.6). The temporal pulse length of such an electron bunch is given by

$$\tau \equiv \frac{\Delta\phi}{\omega} = \frac{s m_e}{2 l e B_0}. \tag{2.23}$$

From this relation it follows that the temporal pulse length of the electron bunches can be controlled by changing the magnetic field amplitude in the chopping cavity, which, as mentioned in Section 2.2.4, can be changed by varying the input power in the cavity.

However in reality an electron beam with zero divergence is impossible, meaning the beam reaching the aperture has a finite spot size σ. The consequence is that electrons passing through the center of the cavity at a phase $|\phi| > \frac{s m_e \omega}{4 l e B_0}$ might still pass through the aperture. In order to take this into account, an effective hole size s_{eff} can be defined. The electrons with the largest divergence are half a spot size removed from those with no divergence. If an electron's corresponding phase would land it less than half a spot size away from the aperture hole, it might still be able to pass through. Since this is valid for both the upper and lower edge of the hole, the effective hole size is

$$s_{\text{eff}} = s + 2 \cdot (\frac{\sigma}{2}). \tag{2.24}$$

Changing the hole size in Eq. 2.23 and using some realistic values results in a temporal pulse length of $\tau = 4.1$ ps for $B_0 = 1.4$ mT, $l = 0.1$ m, $s = 100\,\mu$m, $\sigma = 100\,\mu$m, $f = 3.0$ GHz and $v_z = 9.8 \cdot 10^7$ m/s

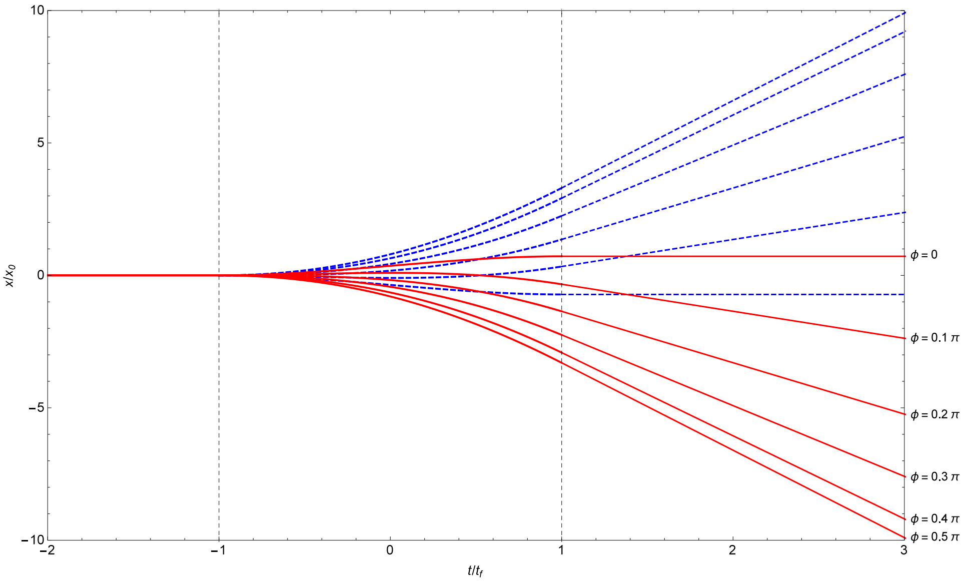

Figure 2.5: The dimensionless transverse electron position as it passes through a TM_{110} cavity. The cavity position spans the range $t/t_f \in [-1, 1]$ with $x_0 = \frac{e B_0 v_z}{m_e \omega^2}$. The blue dashed lines correspond to a π phase shift compared to the solid lines.

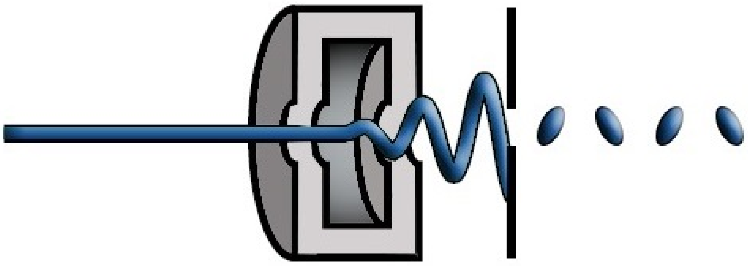

Figure 2.6: The principle of chopping. By placing a slit behind a TM_{110} cavity, only a certain part of the continuous electron beam will pass through, creating a train of electron bunches.

2.3.2 Compression cavity

As was mentioned in Section 2.2.2, electrons travelling along the z-axis through a TM_{010} cavity interact only with the longitudinal electric field. By using that field to decelerate the front of an electron bunch while accelerating the rear, the electron bunch gets compressed. This compression is essentially due to the time-dependent change of longitudinal momentum

$$\Delta p_z = -e \int_{-\infty}^{\infty} E_z \, \mathrm{d}t. \tag{2.25}$$

Assuming that the transverse size of the electron bunch is sufficiently small, a first order expansion of Eq. 2.2 results in

$$E_z(t) = E_0 \cos(\omega t + \phi), \tag{2.26}$$

with ϕ a phase offset. Assuming the change in momentum of the electrons while passing through the cavity is small so that v_z can be regarded as constant, the electron position can be written as $z \approx v_z t + \zeta$ with ζ the distance with respect to the center of the electron bunch. Eq. 2.25 then becomes

$$\begin{aligned} \Delta p_z &= -\frac{e}{v_z} \int_{-\infty}^{\infty} E_0 \cos\left(\omega \frac{z-\zeta}{v_z} + \phi\right) \mathrm{d}t \\ &= -\frac{e}{v_z} \int_{-\infty}^{\infty} E_0 \left[\cos\left(\frac{\omega z}{v_z}\right) \cos\left(-\frac{\omega\zeta}{v_z} + \phi\right) + \sin\left(\frac{\omega z}{v_z}\right) \sin\left(-\frac{\omega\zeta}{v_z} + \phi\right)\right] \mathrm{d}t. \end{aligned} \tag{2.27}$$

In general, an effective cavity length can be defined as

$$L_c \equiv \int_{-\infty}^{\infty} \frac{E(z)}{E(0)} \cos\left(\omega \frac{z}{v_z}\right) \mathrm{d}t, \tag{2.28}$$

with $E(z)$ the position dependent electric field strength. Approximating the electric field in the TM_{010} cavity with a rectangle function of height E_0 and length d, this can be simplified to

$$L_c = \int_{-d/2v_z}^{d/2v_z} \cos\left(\omega \frac{z}{v_z}\right) \mathrm{d}t. \tag{2.29}$$

The right term in the brackets in Eq. 2.27 is an odd term and does not contribute to the integral. Assuming that the duration of the bunch is much smaller than the period of the electric field, i.e. $\zeta/v_z \ll 1/\omega$, and applying Eq. 2.29 yields

$$\begin{aligned} \Delta p_z &= -\frac{eE_0L_c}{v_z} \cos\left(-\omega\frac{\zeta}{v_z} + \phi\right) \\ &\approx -\frac{eE_0L_c}{v_z} \left(\cos(\phi) + \omega\frac{\zeta}{v_z}\sin(\phi)\right). \end{aligned} \tag{2.30}$$

The bunch compression this momentum change is able to cause, can be regarded as longitudinal focusing with the longitudinal focusing power defined as[26]:

$$P_L \equiv \frac{1}{f_L} \equiv -\frac{1}{v_z}\frac{\partial \Delta v_z}{\partial \zeta} = -\frac{1}{v_z}\frac{1}{\gamma^3 m_e}\frac{\partial \Delta p_z}{\partial \zeta}. \tag{2.31}$$

Combining Eq. 2.30 and Eq. 2.31 leads to the expression for the longitudinal focusing power:

$$P_L = \frac{eE_0L_c\omega}{m_e\gamma^3 v_z^3}\sin(\phi), \tag{2.32}$$

with

$$\gamma = \left(1 - \left(\frac{v_z}{c}\right)^2\right)^{-1/2} \tag{2.33}$$

the Lorentz factor. This focusing power describes the behaviour of the TM_{010} cavity as a lens.

2.3.3 Beam parameters

In order to get more insight into the beam properties a phase space description is often used. Since our interests lie in the longitudinal properties, each electron in a bunch will be represented in phase space by its position relative to the center of the bunch and its relative normalized velocity coordinate, (z, z'), as defined in Section 2.1.1. These coordinates for all the electrons will form an ellipse which can be described by

$$\varepsilon = \hat{\gamma} z^2 + 2\hat{\alpha} z z' + \hat{\beta} z'^2, \tag{2.34}$$

where $\hat{\gamma}$, $\hat{\alpha}$ and $\hat{\beta}$ are the Twiss parameters, which relate through $\beta\gamma = 1 + \alpha^2$, and ε the geometrical emittance of the beam[27]. The emittance in transversal directions is a measure of beam quality, where a lower emittance means a better focusability and thus a smaller spot size. The same is true for the longitudinal equivalent: a lower emittance means an electron bunch can be compressed further, resulting in a smaller longitudinal pulse length. Furthermore, the waist of a beam is defined as the point at which the beam width is the smallest. The longitudinal equivalent of this is the position of the center of the bunch when the bunch length is the smallest.

The Twiss parameters allow for a description in matrix formalism by rewriting Eq. 2.34 into

$$\begin{pmatrix} z \\ z' \end{pmatrix}^T \sigma^{-1} \begin{pmatrix} z \\ z' \end{pmatrix} = 1 \tag{2.35}$$

with the beam matrix given by

$$\sigma = \varepsilon \begin{pmatrix} \hat{\beta} & -\hat{\alpha} \\ -\hat{\alpha} & \hat{\gamma} \end{pmatrix} \tag{2.36}$$

The electron bunch will first travel from a waist a distance L_1 towards the compression cavity. The compression cavity will be regarded as a thin lens with focal length f as given by the reciprocal of Eq. 2.32. After the compression cavity, the bunch travels a distance L_2 to another waist. Translated to matrix formalism means that the bunch starts with $\sigma_0 = \varepsilon \begin{pmatrix} \hat{\beta}_0 & 0 \\ 0 & \hat{\gamma}_0 \end{pmatrix}$, since $\hat{\alpha} = 0$ in the waist. The drift-lens-drift system is given by a transformation matrix $M = D_2 L_f D_1$ with the lens matrix given by $L_f = \begin{pmatrix} 1 & 0 \\ -\frac{1}{f} & 1 \end{pmatrix}$ and a drift matrix given by $D_1 = \begin{pmatrix} 1 & L_1 \\ 0 & 1 \end{pmatrix}$. The resulting beam parameters can be acquired from $\sigma_M = M \sigma_0 M^T$. The beam size at the end of the system is then given by[28]

$$\sigma_z = \sqrt{\varepsilon \hat{\beta_M}} = \sqrt{\frac{(f - L_2)^2 \sigma_{z_0}^2}{f^2} + \left(L_1 + L_2 - \frac{L_1 L_2}{f}\right)^2 \sigma_{z'_0}^2}, \tag{2.37}$$

making use of $\hat{\beta}_0 = \sigma_{z_0}^2 / \varepsilon$ and $\hat{\gamma}_0 = \sigma_{z'_0}^2 / \varepsilon$, where σ_{z_0} and $\sigma_{z'_0}$ are the initial longitudinal root-mean-square (rms) bunch size and divergence. Assuming the initial beam has a low velocity spread, the smallest obtainable longitudinal rms beam size $\sigma_{\min} = L_2 \sigma_{z'_0}$ is obtained from Eq. 2.37 when $f = L_2$.

With the goal of EELS being able to measure differences in energy, it is necessary to relate this minimum beam size to the energy spread of the beam. Using Eq. 2.33 and the kinetic energy $E_k = m_e c^2 (\gamma - 1)$, the longitudinal velocity of an electron can be written as

$$v_z(E_k) = \frac{c\sqrt{E_k}\sqrt{E_k + 2m_e c^2}}{E_k + m_e c^2}. \tag{2.38}$$

Taking the first order expansion of $v_z\left(E_k+\sigma_E\right)$ around $\sigma_E=0$ yields the following relation between the rms spread in velocity and the rms spread in kinetic energy:

$$\frac{\sigma_E}{E_k} \approx (\gamma+\gamma^2)\frac{\sigma_{v_z}}{v_z}. \tag{2.39}$$

Substituting $\sigma_{v_z}/v_z = \sigma_{z_0'}$ and $\sigma_{z_0'} = \sigma_{\min}/L_2$ results in the required relation

$$\frac{\sigma_E}{E_k} \approx (\gamma+\gamma^2)\frac{\sigma_{\min}}{L_2}. \tag{2.40}$$

2.3.4 Waist scan description

In order to investigate the performance of the compression cavity as well as to obtain certain beam parameters, a waist scan will be performed. This section will provide a short description of a waist scan.

As mentioned in Section 2.3.2, the compression cavity acts as a longitudinal lens. This lens will create a beam waist at a distance determined the focusing power of the compression cavity as well as the beam parameters at the waist a distance L_1 in front of the compression cavity, where Eq. 2.32 shows that the focusing power is linearly dependent on the electric field amplitude in the compression cavity. Thus if the electric field amplitude is decreased, the focusing power decreases and the waist will move further away. This way the region around the longitudinal waist can be scanned through, with Eq. 2.37 describing the longitudinal size of the beam a distance L_2 from the compression cavity. There are two points of interest in this function. The first is when the focal length of the cavity is equal to the distance L_2. This results in the expression

$$\sigma_z(f=L_2) = \sigma_{\min} = \sqrt{L_2^2\sigma_{z_0'}}, \tag{2.41}$$

from which the initial longitudinal divergence $\sigma_{z_0'}$ can be obtained. The second point of interest is when the compression cavity is turned off. This means the focusing power goes to zero and the focal length to infinity:

$$\lim_{f\to\infty}\sigma_z = \sqrt{\sigma_{z_0}^2 + (L_1+L_2)^2\sigma_{z_0'}}, \tag{2.42}$$

from which the initial rms spread in bunch length can be obtained. With both the longitudinal divergence and spread in bunch length known, the emittance is calculated as $\varepsilon = \sigma_{z_0}\sigma_{z_0'}$. However, a different definition for the longitudinal emittance will be used in this thesis, which is given by $\varepsilon_z = \sigma_E\sigma_{t_i}$ in units of s·eV, and can be calculated using Eq. 2.39 and $\sigma_{t_i} \approx \sigma_{z_0}/v_z$, with σ_{t_i} the rms spread in the initial temporal pulse length.

2.4 The physics of EELS

In Section 1.2 it was mentioned that when electrons interact with a specimen the direction of their momentum changes and they can lose some of their energy. The electrons that do not scatter on the sample naturally do not lose any energy and these electrons will end up in the zero-loss peak of the energy loss spectrum. Those that do scatter can be divided into two groups: *elastic* and *inelastic* scattering.

In elastic scattering the incident electron interacts with an atomic nucleus. As the nuclear mass is much higher than the rest mass of an electron the energy exchange is negligible. These electrons will therefore also end up in the ZLP of the energy loss spectrum. However due to the high concentration of charge in the nucleus, the electric field surrounding it is relatively strong and electrons can be deflected at large angles, also called Rutherford scattering. When this angle exceeds 90° the process is called backscattering. See Fig. 2.7a. Most electrons however will travel further from the nucleus. Due to the inverse square law and shielding of the nucleus by atomic electrons, the electric field will be much weaker and deflection angles will be much smaller. Since many calculations up to now at some point use a small angle approximation (SAA), it is imperative that this is still valid after scattering on the sample. From the cross section of the elastic scatter event an angular width of the scattering distribution can be obtained and is given by[29]

$$\theta_e \approx \frac{Z^{1/3}}{k_0 a_0}, \tag{2.43}$$

with Z the atomic number, k_0 = the electron wavenumber and $a_0 \approx 53 \cdot 10^{-12}$ m the Bohr radius. For 30 keV electrons passing through carbon ($Z = 6$) this results in deflection angle of $\theta \approx 39$ mrad, which is sufficiently small for the SAA.

In inelastic scattering the incident electron interacts with either inner- or outer-shell electrons (see Fig. 2.7b and c). Both types of atomic electrons can undergo single-electron excitation. In this case an electron is excited to a state above the Fermi level, since all states below this level are occupied. As the total energy of such a collision must be conserved, the incident electron will lose the same amount of energy as the atomic electron has absorbed. For inner-shell electrons, this energy is typically hundreds of electronvolts. The excess energy of the highly excited atomic electron is then quickly liberated by filling the vacant hole it left through a de-excitation process, either by the emission of a photon (x-ray) or as kinetic energy of another atomic electron (Auger emission).

The initially outer-shell electrons can lose their energy in the same manner. However, since less energy was transferred in this collision the emitted photon would be in the visible region. Still, most downward transitions are radiationless, which causes the excess energy to be deposited as heat. Electrons excited from the outer shell also may have gained enough energy in the collision to exceed the vacuum level of the material. The excited electron is then emitted as a secondary electron.

Whereas inelastic scattering from outer-shell electrons is visible as a peak in a typical energy loss spectrum, inner-shell excitations are represented by edges: a sharp rise, corresponding to

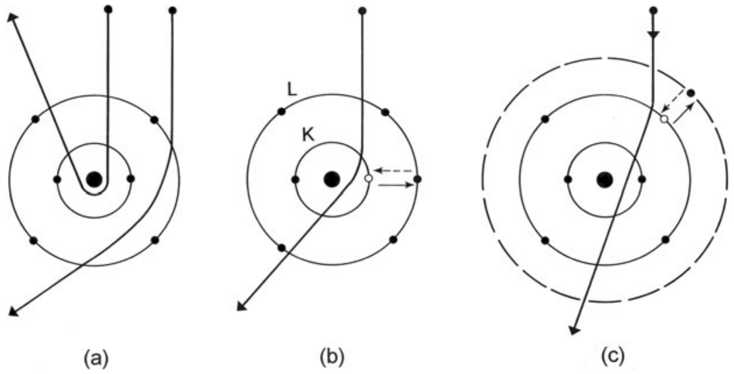

Figure 2.7: A classical (particle) view of electron scattering by a single atom (carbon). (a) Elastic scattering is caused by Coulomb attraction by the nucleus. Inelastic scattering results from Coulomb repulsion by (b) inner-, or (c) outer-shell electrons, which are excited to a higher energy state. The reverse transitions (de-excitation) are shown by dashed arrows. *From* [14].

the binding energy of the relevant atomic shell, followed by a slow drop superimposed on the smoothly decreasing intensity.

Inelastic scattering on outer-shell electrons does not only happen in single-electron excitation. When the incident electron displaces an outer-shell electron through a repulsive Coulomb interaction, the vacant hole left by the outer-shell electron is a region of net positive charge behind the incident electron, slowing it down. The displaced outer-shell electron may induce a longitudinal wave of net positive and negative charged regions called plasma wake oscillations. This excitation can also be described by a pseudo-particle called a plasmon with energy $E_p = \hbar\omega_p$, which is usually in the range of 5–30 electronvolt (eV)[14]. Here $\hbar$ is the reduced Planck constant and ω_p the plasmon frequency. The plasmon peak is also visible in an electron energy loss spectrum.

As inelastic collisions are the main topic of interest in EELS, it is important that the scattering angles following these collisions allow the use of the SAA. From the cross section of the scattering event a scattering distribution can be obtained. This is a Lorentzian function whose FWHM is the characteristic angle[29]

$$\theta_i = \frac{E_L}{\gamma T}. \tag{2.44}$$

Here E_L is the energy lost by the incident electrons in the collision and $T = m_0 v_0^2/2$ is the non-relativistic incident energy. For 30 keV electrons losing 30 eV, this amounts to an angular width of $\theta_i = 2$ mrad, which is even smaller than elastically scattered electrons. This means that the majority of the electrons will scatter at small angles, justifying the use of the small angle approximation.

Chapter 3

Experimental Setup

In this chapter the ToF-EELS beam line setup will be discussed. First a short overview of the two-cavity setup will be given as some details will be important for the requirements of the three-cavity setup design. In order to improve the energy resolution of the ToF-EELS method, a TM_{010} cavity will be inserted, which is described in Section 3.2. This section will also describe the reimplementation of the streaking cavity, as well as provide a description of the peripherals that are used to control the different parts of the setup. Section 3.3 will report on the procedure to align the electron beam through all the beam line elements.

3.1 Two-cavity setup

The first components of the experimental setup are the electron gun and focusing column, both taken from a 30 keV XL-30 SEM. The electron gun uses a tungsten filament as a thermionic emitter and the focusing column holds several computer operated magnetostatic lenses with which the beam can be manipulated. This lens system consist of two pairs of steering coils to shift and tilt the beam, followed by a condenser lens to control the current of the beam by focusing near an aperture. Behind this aperture are two pairs of steering coils which can again adjust the beam position and direction, after which a final lens is used to create a focus somewhere in the beam line. An overview of the electron gun and the focusing column is shown in Fig. 3.1. It was shown before that the chopping cavity, which is placed 0.21 m after the focusing column, causes emittance growth which would be maximized for a collimated beam entering the chopping cavity when the magnetic field is zero[22]. The solution to this was to focus the beam inside the center of the chopping cavity, which results in minimal emittance growth at the zero phase.

Approximately 10 cm after the chopping cavity a 10 μm slit is present, behind which a sample holder is placed. Following the sample holder is a drift length of 1.45 m after which the streaking cavity is placed. A design drawing of the streaking cavity is shown in Fig. 3.2. Approximately 0.5 m after the streaking cavity is a TVIPS TemCam-F216 detector[30].

Along the beam line there are several sets of steering coils used to direct the beam, as well as a solenoid to transversally focus the beam onto the detector. There are also multiple phosphor screens to help align the setup. The entire setup is held at vacuum by rotary pumps and turbomolecular pumps (TMP), while the pressure is measured at three different positions with Leybold TR-211 Thermovac Pirani vacuum sensors. These sensors allow measurements down to a pressure of $5 \cdot 10^{-4}$ mbar. This pressure is sufficiently low to perform EELS measurements, but it does not show the final pressure. While lower pressure vacuum sensors are widely available,

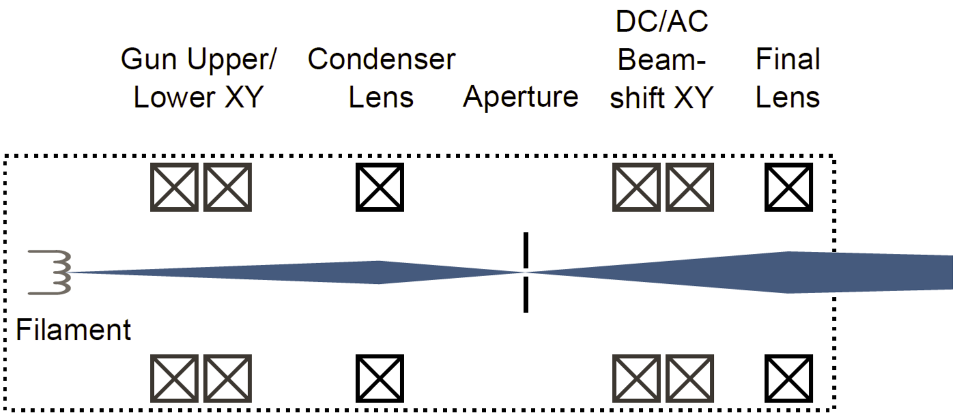

Figure 3.1: Schematic of the electron gun and the focusing column taken from a 30 keV XL-30 SEM. *From* [17].

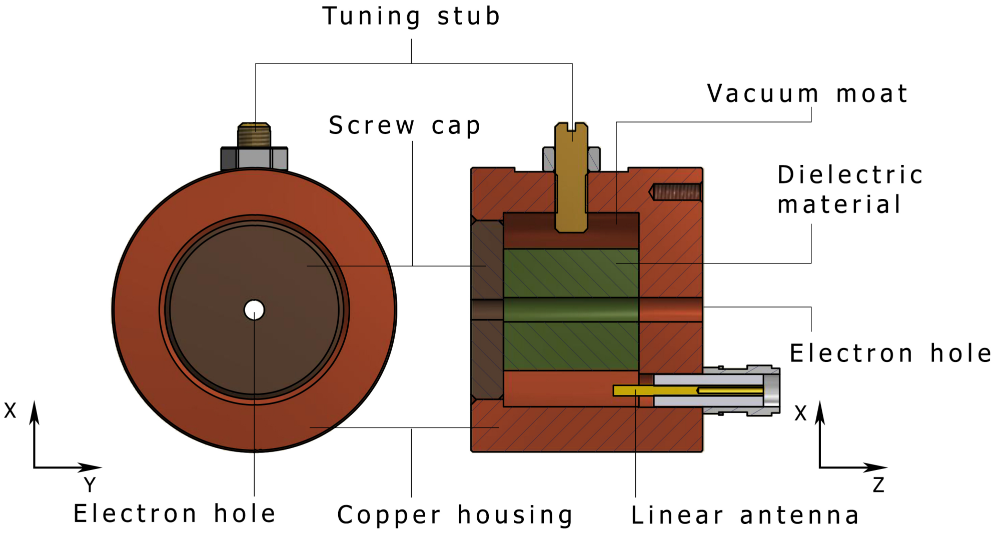

Figure 3.2: Design drawing of the optimized TM_{110} cavity. The z-axis runs through the electron hole. The dimensions are specified in Fig. A.2.

the ones we currently have available have strong magnetic fields that would make it impossible to do EELS, so these are never permanently installed in the setup. An overview of the two-cavity setup is shown in Fig. 3.4. Not shown in this overview is the coil surrounding the entire setup. The Earth's magnetic field, although small in magnitude, influences the electrons along the entire beam line. As the main component of the Earth's magnetic field is downwards, a coil surrounds the entire setup to counteract this. No account has to be taken for the North-to-South component of the Earth's magnetic field, as the setup is oriented in this direction. During the project the single loop coil was replaced with a four loop coil so a lower amperage current supply could be used.

3.2 Three-cavity setup

Compression cavity placement

In creating the new design, the position of the compression cavity is first considered. An important thing to note about the two-cavity setup as shown in Fig. 3.4 is that although the previous position of the streaking cavity is mentioned, it is not actually present. This is due to another experiment taking place at this setup, which has to be able to continue parallel to the ToF-EELS experiment, imposing two relevant constraints on the new design. The first is that the other experiment requires a beam blanker not too close before the third large vessel, as well as an aperture close to and in front of the beam blanker, which is an important restriction for the placement of the compression cavity. The second restriction is of importance for the placement of the streaking cavity and will be discussed later. The beam blanker, which will become important later on in this thesis, will also be discussed later in this chapter.

As explained in Section 2.1.2, using a compression cavity to separate the electron energies longitudinally should result in minimal overlap between the different energies, provided that the resolution is not limited by the beam emittance. If this is not the case, Eq. 2.40 shows that with a given energy spread, the bunch length in the focus increases with a larger distance L_2 between the compression cavity and the streaking cavity, resulting in a better separation of the energies. This would mean the ideal place for the compression cavity is right after the second vessel, maximizing L_2 (moving the second vessel itself would create other technical difficulties and as such was not considered). A consequence however would be that either the distance between the beam blanker and the accompanying slit would increase or that the beam blanker be placed closer to the third vessel, depending on whether the cavity is placed between or in front of the blanker and its slit. As this would be troublesome for the other experiment, the compression cavity is placed directly behind the beam blanker, resulting in a distance of $L_2 \approx 0.93\text{m}$. This means that L_2 is approximately 13% smaller compared to the ideal placement. However, the resolution is not expected to be limited by the beam emittance and even if it is, the resulting energy resolution should still be sufficient for a proof of concept.
Because the compression cavity, as shown in Fig. 3.3, is built with Klein Flange or KF flanges while the rest of the setup is constructed with ConFlat (CF) flanges, two adapter pieces surround the cavity to connect it to the other components. Due to the added length because of both the TM_{010} cavity and the adapter pieces, some extra space has to be made. This is done by removing the valve that is located directly behind the second vessel and by removing the crosspiece that holds the slit in front of the beam blanker and moving the slit to the second vessel. While this does increase the distance between the slit and blanker by a factor of ~4, this should still be workable for the other experiment.

Streaking cavity placement

Next the placement of the streaking cavity is considered, for which there are two major requirements. One of these is the second constriction from the other experiment that was mentioned previously. For that experiment a blockade in front of the detector, such as a cavity with only a 2.5 mm entry hole, is not allowed. The final design must thus make possible the easy addition and removal of the streaking cavity from the beam line. While a motorized retractable stage would be ideal for this, the one our group possesses was in use at the time. Instead is opted to just vent that part of the setup each time it had to be removed. While not the most ideal solution, our system does not have high vacuum requirements with pressures below 10^{-3} mbar being sufficient, meaning the entire process would not take much more than an hour.

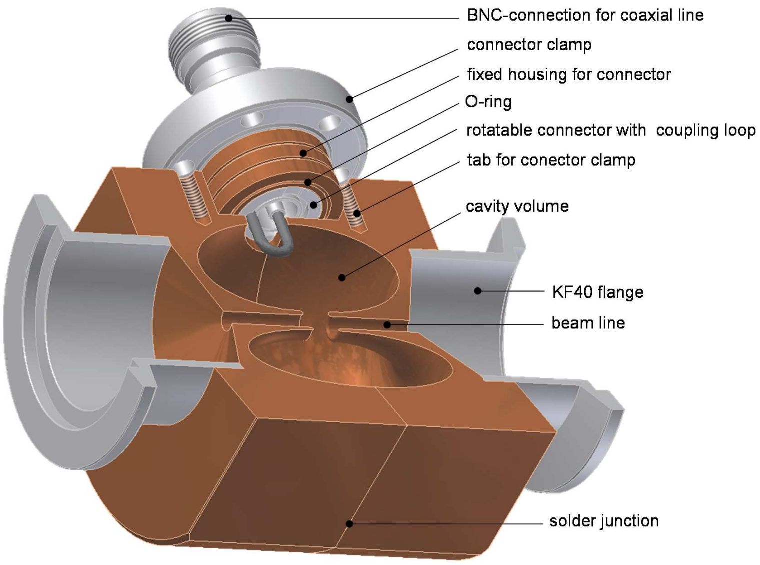

Figure 3.3: Design drawing of the optimized TM_{010} cavity. The dimensions are specified in Fig. A.1. *From* [23].

The second requirement for the streaking cavity placement lies in the fact that the detector is less than 17 mm removed from the edge of the table upon which the setup is mounted. While it is possible to let the detector extend slightly beyond the table, it is undesirable to expose such a vital and expensive part of the experiment to potential harm. As such the new design must not lengthen the setup by more than 17 mm.

The vacuum component that would hold the streaking cavity would have to fit a CF100 flange on one side and a CF40 flange on the other side and due to the dimensions of the cavity has to be at least the size of CF63, where the number behind CF specifies the nominal inner diameter of the flange in mm. Considering these requirements a CF63 6-way cube was chosen. Although with a cube it is impossible to use a thin reducer flange to a size larger than the cube itself, the reduced dimensions of a cube compared to a crosspiece result in the smallest increase of length, leading to the detector being just about even with the edge of the table depending on how far the small bellows is compressed. The use of a vacuum cube also keeps open the option to use the motorized retractable stage.

After all the changes involved in adding the compression and streaking cavity were made and ensuring each component was still aligned with the electron gun, a high vacuum pressure sensor was temporarily installed, measuring a final pressure of $3.2 \cdot 10^{-6}$ mbar. The distance between the compression and streaking cavity was measured to be $L_2 \approx 0.93\,\text{mm}$, while the distance between the streaking cavity and the detector is $L_d \approx 0.55\,\text{m}$. An overview of the three-cavity setup is shown in Fig. 3.5.

Beam control

There are several devices, other than the cavities, used to control the electron bunches along the beam line. An important component is the solenoid used to transversally focus the electron bunches onto the detector. The solenoid is mounted onto a stage allowing for 3D positioning around the drift space tube, which is placed behind the compression cavity and in front of the third vessel. The setup also has sets of steering coils in multiple locations, which are capable of shifting the direction of the beam both horizontally and vertically. One set of steering coils consists of four coils, two for each direction. The sets of steering coils are often placed in pairs, just like the steering coils in the focusing column, so that both the transverse beam position and angle can be controlled. Finally there are phosphor screens positioned in the first through third large vacuum vessels. Through a view port in these vessels, the position of the beam can be checked on the phosphor screen in order to align the setup.

Beam blanker

Although the beam blanker initially was kept in the setup only because of a different experiment, later on in this thesis it will become a crucial tool in performing measurements. As such a brief overview of the blanker will be given here.

The beam blanker consists of two 1 by 4 cm conductive plates separated by 0.4 cm, where the long side is oriented along the beam direction. While the potential on one of these plates is held at ground with respect to the rest of the setup, the other plate can be charged. Using a pulse generator, small pulses of a desired length and frequency are sent to the beam blanker, generating a uniform electric field between the plates corresponding to the sent pulse. The electric field exerts a force on the electrons passing through, pushing them towards the charged plate and thereby giving them a slightly different angle than when the blanker is turned off. This will later on allow for separation of certain electron bunches from the rest.

However, due to the small dimensions of the blanker plates the electric field quickly becomes non-uniform when deviating from the z-axis. This causes some issues with alignment, which will be discussed in Section 3.3.

Power supplies

The components in the beam line also need to be powered and operated in some way. Most of these only require a power supply, such as the steering coils and solenoid. While this seems like a trivial thing, many devices create (AC) magnetic fields that disturb the beam. While this will be discussed in more detail in Section 5.2, it was found that a Delta Elektronika Power Supply ES 030-5 causes no visible disturbance to the beam regardless of proximity or orientation and is used for most of the devices. The steering coils are powered by AccTec B.V. bi-polar current sources, which also do not interfere with the electron beam.

Temperature control

The devices needed for the cavities are a bit more extensive. As mentioned in Section 2.2.3, the resonant frequency of the cavity is dependent on the temperature, where a change in resonant frequency changes the amount of coupling and thus the power transferred to the cavity, which could change the temperature again. Therefore it is required to actively stabilize the cavity temperature.

Earlier measurements on this particular TM_{010} cavity showed that a field amplitude of 2 MV/m is obtained for 43W of RF power[26]. Using Eq. 2.32 with an effective cavity length of 6 mm and the scaling between electric field amplitude and the stored energy as described in Section 2.2.4, the required power for the compression cavity to create a waist at a distance of 0.93 m is approximately 40 mW. Combining this relatively low power with the fact that the compression cavity has thick copper walls, meaning outside influences are less significant, reduces the requirements of the temperature stabilization. The end result is a controller that powers a heating element, while a fan cools a heat sink attached to the bottom of the cavity. Considering that the cavity is part of the beam line and thus in contact with air, the cavity is surrounded by insulating material and a PVC housing to decrease the influence of the ambient temperature.

Whereas the compression cavity is exposed to air, the TM_{110} cavities are suspended in vacuum, therefore removing the need of isolation. Due to its design however, the required temperature stability is much higher. For this two water coolers were custom built. One of these uses an NTC-resistor and can stabilize the temperature of the cavity to a few mK. The other water cooler uses a thermocouple and thus performs slightly worse than the one using an NTC-resistor, yet is still able to stabilize the temperature sufficiently.

RF infrastructure

In order for the cavities to operate at the desired frequency and power, a new 50Ω RF infrastructure was designed (see Fig. 3.6). The process starts with a Mini-Circuits ZX953060C+ Voltage Controlled Oscillator (VCO) which, when supplied with the correct voltage, will generate a frequency of 2.9985 GHz (which can be checked with a PFM3000 Frequency Counter) at approximately 3 dBm. This signal first passes a switch, splitter and programmable attenuator. The switch allows for the use of an RF source which is synchronized with a laser, although this is currently not used in the experiments. The signal is then fed to a custom built signal splitter box where it is first amplified by 12 dBm. To ensure the power and phase of the signal supplied to each cavity can be manipulated individually, the signal is then split four ways. The 12 dBm pre-amplification ensures enough power is supplied to each of the four paths. The reason the signal is split four ways while there are only three cavities, is due to future plans to add a fourth cavity. More details can be this found in Section 6.2.1.
From Eq. 2.32 it directly follows that the focusing power of the compression cavity is dependent on the electric field amplitude, which in turn is dependent on the input power. It is therefore necessary to be able to change this input power as desired. Voltage variable attenuators (VVA) allow for any attenuation within a certain range and would at first sight seem to be the ideal choice. The two major downsides to VVAs are that the attenuation-voltage behaviour is non-linear and its stability is dependent on the stability of the voltage supply. Instead is opted for a digital step attenuator (DSA). The attenuation of such a DSA can be controlled with our custom software and has a range of 0 to 30 dBm with steps of 0.25 dBm, resulting in a maximum deviation from ideal focal length of 1.4%, corresponding to approximately 0.04 eV for a minimum spot size of 31.3 μm.

After the individual signals leave the splitter box the lines to the first and second cavity pass through their own phase shifter to ensure the electrons enter each cavity at the proper phase. Setting these phase shifters correctly is relatively easy and will be explained in Section 3.3.

Before the signals are sent through a Mini-Circuits ZHL-16W-43+ power amplifier, they are first attenuated with fixed attenuators. This is done in order to ensure the signal is in the right power range after amplification so the entire range of the DSA can be utilized. After the amplifier a hardware scheme with a corresponding software program was made to allow a single power sensor to measure the power forwarded to and reflected from two cavities. This is achieved by passing the amplified signal through a Meca Electronics 722S-40-3.100R Dual coupler before being sent to the cavity. This dual coupler has two outputs, one for the total incoming power and one for the reflected power, with an attenuation of 40 dB each. Both these outputs, together with the two outputs from the other dual coupler, are passed to an USB-controlled Mini-Circuits USB-SP4T-63 RF switch whose output is connected to the Mini-Circuits PWR-SEN-6GHS power sensor which can be read out from the computer. With a power input of approximately 40 mW to the cavity, the reflected power will be in the order of 1 mW or 0 dBm. With the 40 dB attenuation of the dual coupler, this will become -40 dBm, well outside the -30 to $+20$ dBm range of the power sensor. In order to ensure accurate measurements for this as well, a $+13$dB Mini-Circuits ZX60-3018G-S+ amplifier was added between the RF switch and the dual coupler output in question. Although this construction with the dual coupler and RF switch allows reading four power outputs with only one Mini-Circuits power sensor, the chopping cavity is connected to a 7020-1-010101 RF Bird power sensor capable of reading out both total and reflected power. This is due to practical reasons.

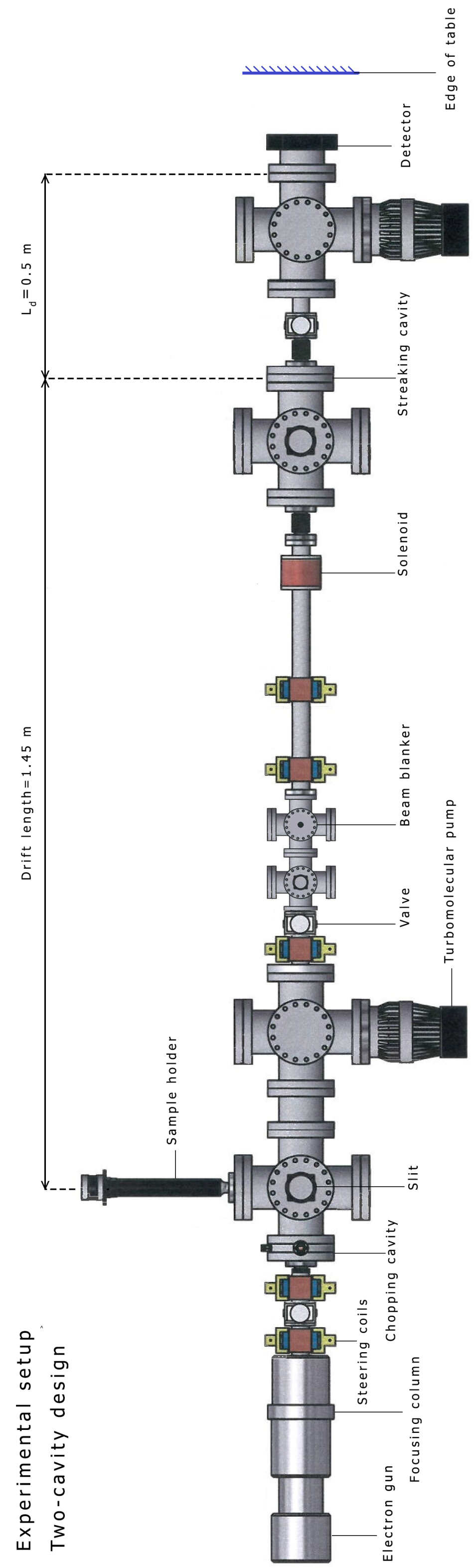

Figure 3.4: The two-cavity experimental setup. The streaking cavity position is indicative, as the cavity is not actually there. Not to scale.

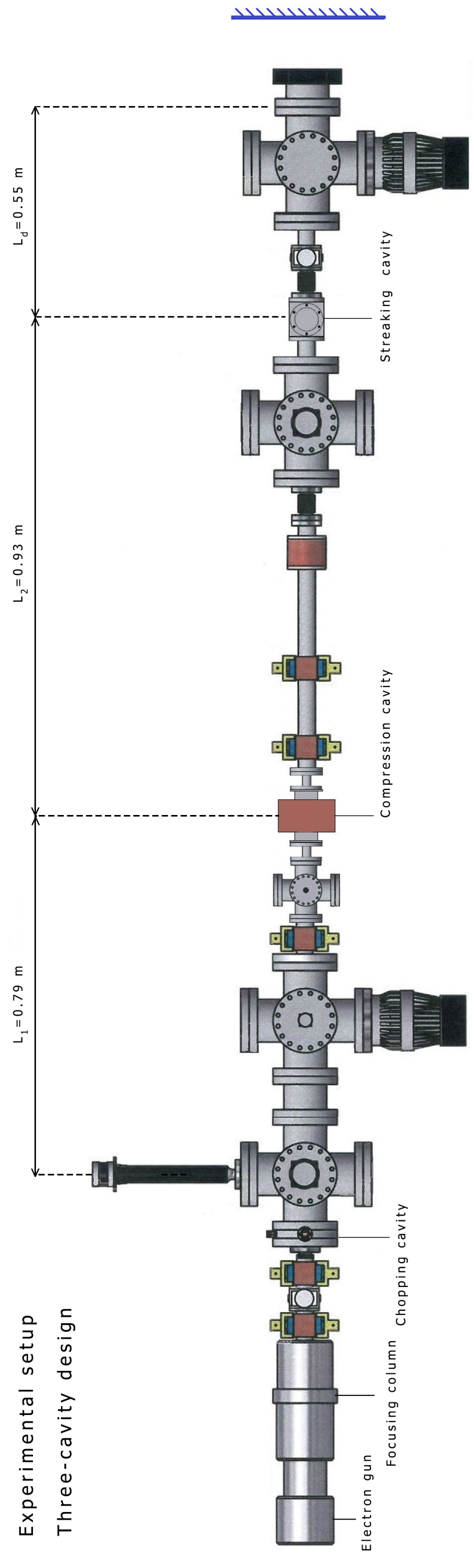

Figure 3.5: The final design for the three-cavity ToF-EELS setup. Not to scale.

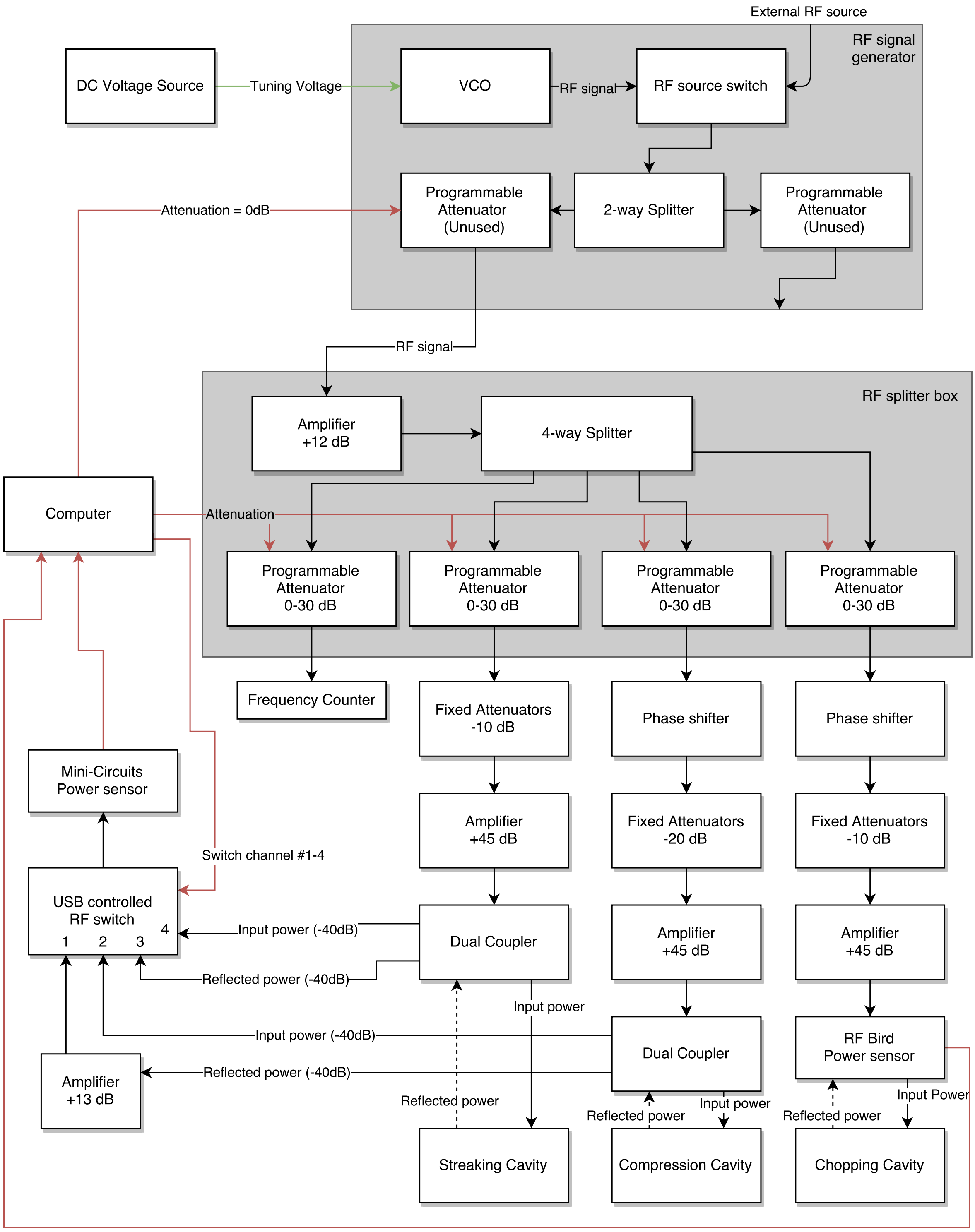

Figure 3.6: Schematic of the RF setup that generates the RF signal and provides it to three cavities with controllable phase and power input. The black arrows represent the RF signal and the red arrows represent a USB connection. The dashed lines connecting a cavity to its previous element is not a cable, but represents the reflected power at the antenna.

3.3 Alignment Procedure

With all the elements present in the beam line, it has become increasingly difficult to properly align the electron beam through each element and onto the detector. This section will describe a systematic method to achieve proper alignment. Most of the transverse alignment in the beam line is performed using sets steering coils, each consisting of four coils, and are usually used in pairs. Whereas one set of steering coils can adjust the angle of the electron beam, two sets are capable of adjusting both the angle and transverse position. These can also be called the position and angle coils, with the angle coils placed behind the position coils.

Earth magnetic field correction

The first part of the alignment is the Earth magnetic field correction, which is done with a four loop coil running around the entire beam line. The downward component of the Earth magnetic field is first measured with a magnetic field meter. Using a current supply, a current is run through the coil in order to counteract the measured magnetic field. This results in a current in the range of 1.7 to 2 A.

Pre-sample transverse alignment

The second part that should be aligned is the focusing column. In order to do this, the electron beam can be aimed through the chopping cavity and onto the phosphor screen attached to the sample holder. The focusing column contains two lenses: the condenser lens and the final lens, both of which have two sets of computer controlled steering coils in front of them. The condenser lens is used to control the amount of current in the electron beam, where a lower current should result in a lower beam emittance. The final lens determines the position of the transversal focus in the beam line. In order to transversally align the condenser lens, it is *wobbled.* This means that the current through the element in question will constantly be varied within a certain range. If the beam is misaligned two things may occur: the spot on the phosphor screen is (partly) cut off, or the position of the electron spot changes. To ensure proper alignment, the Gun upper and lower steering coils (see Fig. 3.1) must be changed until both of these effects are gone for the range of condenser settings that will be used in a measurement. The final lens is aligned in a similar manner with the beamshift steering coils.

The next part is the alignment through the center of the chopping cavity. Varying the current through steering coils in front of the chopping cavity will cause the beam to get cut off at some point due to the edges of the cavity hole. By using the angle coils of the chopping cavity to keep track of the cut-offs, the position coils are used to maximize the distance between two opposite cut-offs. This ensures the beam passes through the center of the chopping cavity. Another visual cue for this is the rate at which the beam gets cut off. For example, if the beam is off-center towards the positive x-direction, the cut-off will happen over a shorter range in the positive x-direction than in the negative x-direction. After the beam position is placed in the center of the chopping cavity, the angle is aligned by setting the electron spot an equal distance from all the cut-offs.

The slit is then inserted to ensure the electron beam passes through it properly. Small adjustments to the steering coils can be made to achieve this. If the electron beam does not pass through the slit, it is not visible on the phosphor screen and can be difficult to find. By turning on the chopping cavity a streak is made, which can aid in finding and aligning the beam through the slit.

Transverse drift space alignment

In the next part of the alignment, the beam should pass through both the beam blanker and the compression cavity before hitting the phosphor screen in the third vessel. In order to find the beam on this screen, the steering coils in front of the beam blanker are wobbled over the entire range of currents available. If the beam is not found after this, more steering coils are employed. Due to the difficulty in aligning the beam properly through both the beam blanker and the compression cavity, steering coils were later added between the two. Even with this, aligning this part of the beam line is troublesome. The best solution to this would be removing the beam blanker, which is not yet possible as it is needed for measurements.

After proper alignment through the beam blanker and compression cavity, the beam should be aligned straight through the center of the solenoid. If the alignment is off-center or at an angle with the z-axis, the spot position on the phosphor screen changes with varying current through the solenoid. Aligning the solenoid properly is an iterative process. First the solenoid angle coils are used to angle the beam in such a way that varying the current through the solenoid between $0\,\mathrm{A}$ and small values ($< 0.1\,\mathrm{A}$) does not change the position of the electron spot on the phosphor screen. Calling this position the zero position, the iterative alignment procedure is as following: First the solenoid current supply is set to a higher value (~0.8 A), moving the spot away from the zero position. The position coils are then used to place the spot back on the zero position. Turning the solenoid off will again move the spot away from the zero position. After that the angle coils are used to place the spot back on the zero position. This process is repeated until the position of the spot changes as little as possible with varying currents through solenoid.

Taking out the phosphor screen, the electron beam might already hit the detector. If that is not the case, a set of steering coils behind the solenoid can be used to aim the beam through the streaking cavity, again using the wobbler to scan the entire range if necessary.
With the electron beam hitting the detector, the two transverse focus positions in the beam line can be set with the final lens and the solenoid. The solenoid is set by minimizing the spot size on the detector, while the final lens is a bit trickier. As mentioned before, the first focus should be placed in the chopping cavity to minimize emittance growth. However the beam size cannot be viewed inside the cavity. Instead, a TEM grid is placed in the sample holder and imaged onto the detector. If the alignment is off, the emittance growth will cause the lines on the TEM grid in one direction to blur. Proper alignment is thus achieved by creating the sharpest image of the TEM grid.
Having the electron beam hit the detector is not sufficient however. Not only is the detector damaged in a few places, a measurement necessary for data analysis is the full length of the streak made by the streaking cavity, as will be explained in Chapter 4. As this streak might not completely hit the detector, two steering coils can be added to place the full streak on the detector.

Cavity alignment

Aligning the three different cavities starts with ensuring they are all at resonance. This is done in two ways: setting the frequency and varying the cavity temperatures. The temperatures of the TM_{110} cavities are regulated by their respective water coolers, while the temperature of the compression cavity can be regulated with the fan speed and the heating element. Setting these temperatures such that the resonant frequencies of the three cavities are close to each other, the tuning voltage supplied to the VCO is set so that all three cavities are coupled sufficiently, which can be monitored with the power sensors.

Properly aligning the phase differences between the three cavities is done with the phase shifters attached to the chopping and compression cavity. Calling the phase at which the magnetic field in the TM_{110} cavities and the electric field in the compression cavity is zero the zero phase, the goal is to get the part of the continuous electron beam that passes through the zero phase of the chopping cavity to also pass through the zero phase of the compression and streaking cavity.
First the phases between the chopping and streaking cavity are aligned. Turning off the chopping cavity and turning on the streaking cavity creates a full streak on the detector. If the chopping cavity is then turned on, electron bunches are created and only a small spot is made on the detector. Shifting the RF phase of the chopping cavity moves this spot along the path which the full streak made. Proper alignment is achieved when the small spot is in the middle of the full streak.
Aligning the phase of the compression cavity happens in a similar manner. If the electron bunch does not pass through the compression cavity at the zero phase, the bunch will gain a net acceleration or deceleration. This causes the electron bunch to arrive at the streaking cavity at a different time and thus a different phase, again moving the electron bunch along the path of the full streak. Changing the RF phase of the compression cavity such that the electron spot is in the same position when the compression cavity is turned on and off thus ensures proper phase alignment.

As shown in Fig. 3.6, the power in the cavities can be set to the desired value by using programmable attenuators. One issue with this however is that if the attenuation is decreased and more power is sent to the cavity, the temperature equilibrium and thus the resonant frequency will change. If this shift in resonant frequency cannot be countered with the water cooler (since this problem does not occur for the low powers used in the compression cavity), the cavity has to be taken out of the setup to adjust the resonant frequency using the tuning stub or screw cap. This means that not the entire range of available powers can be used in a measurement in quick succession. This effect occurred when changing the power in the chopping cavity from approximately 3 W to 6 W, but not when changing it from approximately 3 W to 1 W.
Two small issues were discovered in the operation of the programmable attenuators. One is that between some attenuations the position of the electron spot on the detector seems to change slightly, which might be due to a small phase shift. This can be caused by the path length through the attenuator changing slightly, but this was not investigated. The other issue is that some pairs of consecutive attenuator values actually attenuate the signal by the same amount, i.e. there is no difference between 16 dB and 16.25 dB attenuation. This has also not been investigated. These two issues however do not hinder any measurements in a significant way.

Sample alignment

The final alignment that is necessary when doing EELS is inserting a sample. Since the sample is relatively large compared to the beam size, inserting the sample holder the correct distance is sufficient for proper alignment and as the sample holder is computer controllable, the correct distances are pre-set.

Chapter 4

Results two-cavity ToF-EELS

Before rebuilding the experimental setup to accommodate the compression cavity, the performance of the old setup is confirmed. As mentioned in the previous chapter, minimizing the emittance growth requires the electron beam coming from the gun to be focused inside the chopping cavity. In order to ensure this, a TEM grid is placed in the sample holder. By imaging this TEM grid onto the detector, an under- or overfocus will cause the grid features to become less visible (see Fig. 4.1).

Figure 4.1: Inverted contrast images of a TEM grid on the detector using a pulsed beam for different focal strengths of the SEM final lens. Focal strength of the final lens increases from left to right. From [31].

In order to interpret the detector image in an EELS measurement, the position of an electron on the detector has to be coupled to its energy at the sample. This is done by coupling both of these to the arrival time at the streaking cavity. For this a full streak is made by turning the chopping cavity off. The length of the full streak is then given by

$$\chi_{\text{full}} = \left|2L_d\alpha(\phi = \frac{\pi}{2})\right| = \frac{4eL_dB_0}{m_e\omega}, \tag{4.1}$$

with L_d the distance between the streaking cavity and the detector and $\alpha(\phi)$ the sweeping angle from Eq. 2.21. Assuming the pulse length is small compared to period of the cavity and that the center of the bunch passes through the center of the streaking cavity at the zero phase, the size of the streaked bunch on the detector is given by

$$\chi_{\text{chopped}} = \left|2L_d\alpha(\frac{\omega\sigma_t}{2})\right| = \frac{4eL_dB_0}{m_e\omega}\sin\left(\frac{\omega\sigma_t}{2}\right) \approx \frac{2eL_dB_0\sigma_t}{m_e}. \tag{4.2}$$

Combining Eq. 4.1 and Eq. 4.2 leads to the expression for the rms temporal pulse length of the bunches:

$$\sigma_t = \frac{2\chi_{\text{chopped}}}{\omega\chi_{\text{full}}}. \tag{4.3}$$

In general, spot sizes on the detector in the streaking direction are indicated with a χ while rms bunch lengths and durations in the beam line are indicated with a σ. Having obtained the temporal spread, the rms kinetic energy spread σ_E is then calculated by using Eq. 2.39 and $\sigma_{v_z}/v_z \approx \sigma_t/t_0$, leading to

$$\sigma_E \approx E_k(\gamma + \gamma^2)\frac{\sigma_t}{t_0}, \tag{4.4}$$

with $t_0 = 14.70 \pm 0.02$ ns the average unperturbed flight time of the electrons.

Inserting a cross grating sample containing a polycrystalline gold layer deposited on a carbon film[32], images are taken for two RF phases of the cavity, as well as one image without a sample present (see Fig. 4.2). Averaging the counts along a few lines through the zero-loss and plasmon peak results in an electron energy loss spectrum, as shown in Fig. 4.3. Apparent from these two images is the broader zero-loss peaks found in both the reversed phase spectrum and the sample removed spectrum, which is also taken at the reversed phase. The difference between the two RF phases will be explained later in this chapter. Comparing the reversed phase spectrum and the sample removed spectrum, the emergence of the plasmon peak at approximately 20–25 eV is visible. However, the ZLP of the phase reversed measurement, which is broadened compared to the EELS measurement, covers a large part of the plasmon peak. Fitting the ZLP of the EELS measurement with a Gaussian and taking into account the uncertainty in the unperturbed flight time, an energy resolution of $\Delta E_{\text{FWHM}} = 10.8 \pm 0.2$ eV is obtained using the relation $\Delta_{\text{FWHM}} = 2\sqrt{2\ln 2}\sigma$. This is the value we seek to improve by adding a compression cavity. The uncertainty is in a 1σ interval. Resolutions are given in their FWHM value as the energy resolution of an electron energy loss measurement is defined as the FWHM value of the ZLP. An interesting possibility might be to combine the ToF-EELS method with pump-probe types of experiments. The time resolution of a pump-probe experiment is mainly determined by the pulse length at the sample. From the two-cavity EELS measurement a temporal spread of $\Delta t_{\text{FWHM}} = 2.43 \pm 0.06$ ps at the streaking cavity is obtained, which would be the upper limit to the temporal resolution of a pump-probe experiment, as it includes the pulse broadening in the drift space.

Also apparent from the results of these measurements is the difference between the normal and reversed phase. This can be caused by misalignment of the solenoid. By passing through the solenoid under an angle, z-x correlations in the electron beam can be induced. This z-x correlation either complements or opposes the direction in which the bunches get streaked, resulting in slightly different streaks between the two RF phases. General Particle Tracer (GPT)[33] simulations of an electron bunch for two phases of the streaking cavity are shown in Fig. 4.4, displaying this effect. In order to minimize this effect, the solenoid has to be aligned with much care.

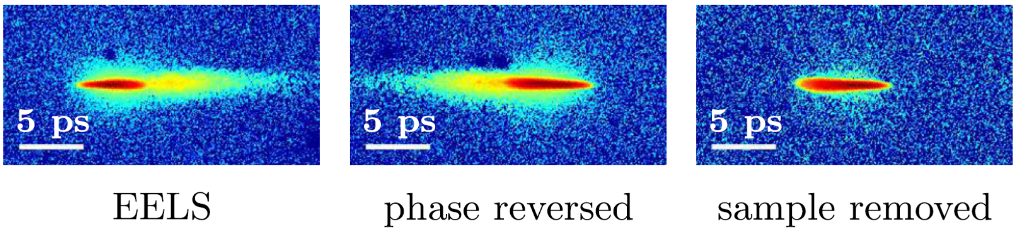

EELS phase reversed sample removed

Figure 4.2: The signal on the detector color coded on a logarithmic scale. From left to right an EELS measurement, the same measurement with the streaking direction of the streaking cavity reversed and a measurement without sample. *From* [31].

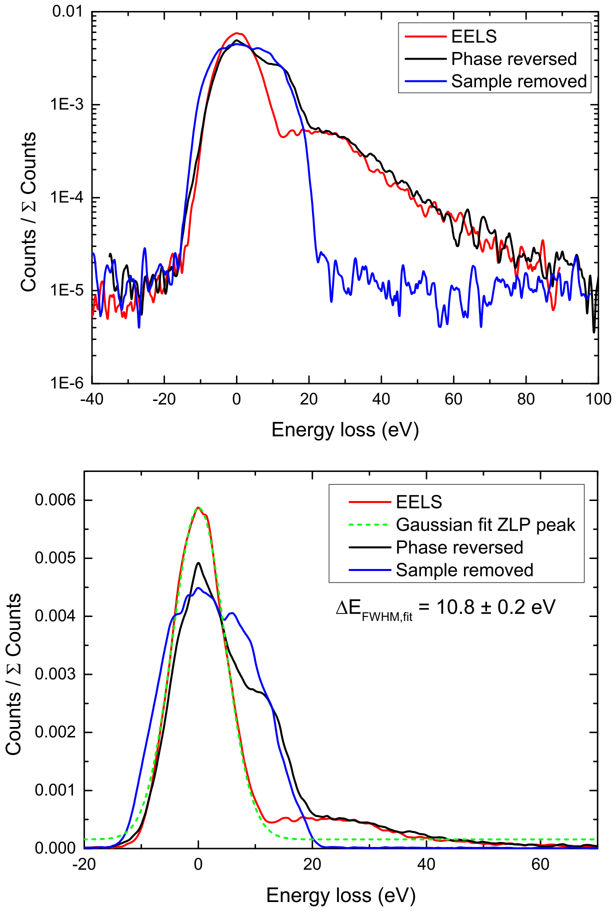

Figure 4.3: The electron energy loss spectra obtained from the images in Fig. 4.2 plotted logarithmically (top) and linearly (bottom). The ZLP of the electron energy loss spectrum has a FWHM of 10.8 ± 0.2 eV from the fit.

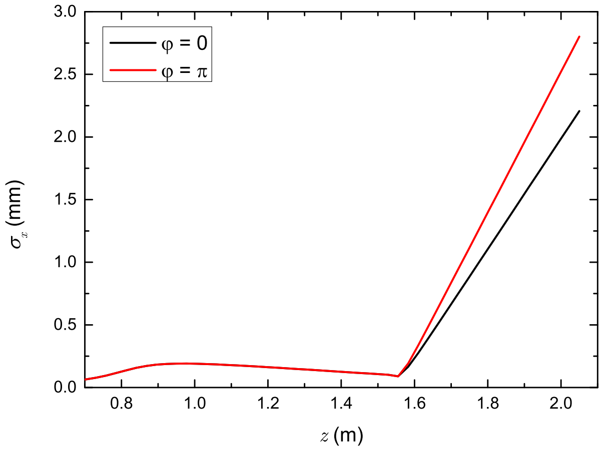

Figure 4.4: GPT simulation of the ToF-EELS beamline for two opposite RF phases of the streaking cavity with the solenoid at $z = 0.81$ m misaligned by a 1 degree tilt about the x-axis. A difference in transverse rms beam size σ_x arises at the streaking cavity placed at $z = 1.55$ m due to the tilt of the solenoid. The detector is placed at $z = 2.05$ m.

Chapter 5

Results beam line with TM$_{010}$ cavity

In this chapter the performance of the compression cavity and its effect on an EELS measurement will be investigated. In Section 5.1 the achievable longitudinal beam quality and pulse lengths will be described, both in an experiment as well as with GPT simulations. Their results show that the experimental setup is not performing as desired and several sources of disturbance are investigated and described in Section 5.2. With some sources of disturbance removed and another circumvented, the performance of the compression cavity and its effects on an EELS spectrum will be reported on in Section 5.3.

5.1 Compression cavity performance

In order to check if the compression cavity performs as expected, a longitudinal waist scan has been made. According to Eq. 2.32, the focusing power and thus the focal length can be adjusted by changing the electric field strength. Varying the focusing power means the longitudinal equivalent of the back focal plane will shift in position. As mentioned in Section 2.2.4 the electric field strength scales with the square root of the energy in the cavity. With this and the focal length scaling with the reciprocal electric field strength, the focal length of the cavity is given by

$$f(P) = L_2 \cdot \sqrt{P_0/P} \tag{5.1}$$

where $L_2 = 0.93 \pm 0.01\,\mathrm{m}$ the distance between the compression and streaking cavity and P the power in the compression cavity with P_0 the power such that the longitudinal waist is placed in the center of the streaking cavity. Eq. 2.37 then describes the behaviour of the bunch length as a function of f.

Just as with the EELS measurement without a compression cavity, there is a need to couple the temporal spread of the bunches in the cavity from Eq. 4.3 to the energy spread of the initial pulses. Using Eq. 2.40 and Eq. 4.3 and assuming $v_z \gg v_x, v_y, \sigma_{v_z}$ such that $\sigma_z \approx \sigma_t v_z$, an expression for the rms energy spread is obtained:

$$\sigma_E = (\gamma + \gamma^2)\frac{2 v_z E_k}{\omega L_2}\frac{\chi_{\mathrm{chopped}}}{\chi_{\mathrm{full}}}. \tag{5.2}$$

A waist scan is then performed by varying the power in the compression cavity and in Fig. 5.1 the result is shown. Comparing the smallest spot size on the detector χ_{min} of the waist scan to $\chi_{\mathrm{min}} = 31.3\,\mu\mathrm{m}$ from the simulations, the result from the measurement is clearly much higher. Using Eq. 5.2 this would mean that the FWHM energy spread of the beam as measured is approximately 29.8 ± 0.5 eV as opposed to the 2.41 eV from simulations. The electron bunch in the simulations had an energy spread of 2.37 eV directly after exiting the slit. After further investigation a pattern was found to emerge around the waist of the beam. As will be shown in the next section, this pattern arises from the electron beam periodically shifting between several different positions within the shutter time of the detector, which explains why the measured spot size does not decrease as much as expected (see Fig. 5.2).

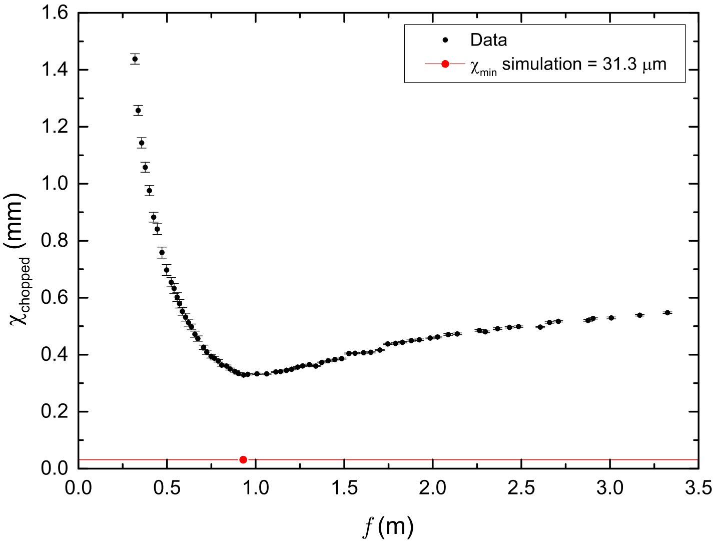

Figure 5.1: Results of the waist scan with $\chi_{\text{full}} = 28.8\,\text{mm}$. Also shown is the minimum spot size obtained in a simulation with $\chi_{\text{full}} = 23.3\,\text{mm}$.

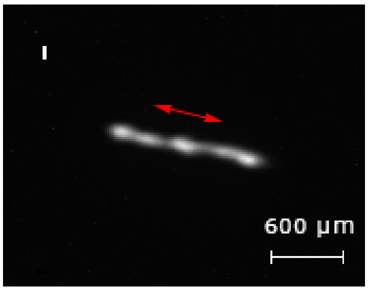

Figure 5.2: The electron spot on the detector at optimal compression of the TM_{010} cavity. The red arrow indicates the streak direction of the streaking cavity. The width of the white line in the top-left corner indicates the expected spot size of 31.3 μm.

5.2 Sources of disturbance

Since the same pattern emerged regardless of the exact alignment, the suspicion arose that one or more devices were emitting AC magnetic fields. In order to estimate the magnetic field amplitude capable of causing this, some approximations are made. First is that the source of disturbance operates at a frequency much lower than 3 GHz, so the magnetic field can be considered constant for one bunch. The second is the small angle approximation, which should be valid since the deviation is about 500 μm over a distance of more than a meter. The force acting on the electrons is then $F = -ev_z B_d$ with B_d the magnetic field amplitude of the component perpendicular to v_z. Integrating this over time once results in the velocity and twice results in the position as function of time. Assuming the magnetic field influences the beam the first Δz meter of the beam line, the deviation Δx_d from the z-axis at the detector is given by

$$\Delta x_d \approx \Delta x(t_1) + (L_\mathrm{T} - \Delta z)\,\frac{v_x(t_1)}{v_z} = \frac{-eB_d}{m_e v_z}\left(\frac{\Delta z^2}{2} + \Delta z\,(L_\mathrm{T} - \Delta z)\right), \tag{5.3}$$

with L_T the total path length of the electrons, $v_x(t_1)/v_z$ the angle of the electrons at t_1 and $t_1 = \Delta z/v_z$ the time the electrons exit the influence of the magnetic field, assuming they enter at $t = 0$. Taking $\Delta z = 0.5\,\mathrm{m}$, a total length of $2.3\,\mathrm{m}$ and a resulting deviation of $500\,\mu\mathrm{m}$, solving Eq. 5.3 for B_d leads to a magnetic field amplitude of approximately $270\,\mathrm{nT}$, which is two orders of magnitude smaller than the Earth magnetic field.

In order to find possible sources of electromagnetic interference, both a flat Faraday 'cup' and an AC magnetic field meter were used. A Faraday cup is a conductive cup, or in this case a flat surface, that gains a net charge due to the incident electrons. The Faraday cup is connected to a sensitive current meter that measures a current proportional to the amount of incident electrons. If the beam fully hits the Faraday cup the DC current can measured. This however did not reveal any oscillations due to AC magnetic fields. Aiming the electron spot partly on the metal surface and partly through a hole in the surface should allow transverse oscillations to be measured. However, while this method does work for measuring the DC current, no AC behaviour was found. This might be due to a lack of precision in the measurement method or that the oscillations are mainly in the longitudinal direction.

By using a AC magnetic field meter, it was revealed that the Leybold Thermovac vacuum gauge controllers models TM20, TM21 and TM22, used to read out the pressure measured by the vacuum sensors, emit relatively large magnetic fields at the utility frequency of 50 Hz. To confirm the effects of these devices, the continuous electron beam was focused directly onto the detector. The initial focused beam spot was found to be non-Gaussian, as shown in Fig. 5.3. Coincidentally, the effects of the several gauges seem to partially counteract each other. This is apparent since moving away, turning off or even plugging into a different outlet the TM21 or TM22 model makes the deformation of the spot much worse, before improving when both those models are turned off (see Fig. 5.4a & b). The effects of the TM20 model were minimal compared to the other two. As the gauges are not necessary during measurements, they can simply be turned off at that time to prevent them from interfering.

Another source of interference is the water cooler for the chopping cavity. Turning it on results in the deformed spot in Fig. 5.4c. As the water cooler cannot be turned off during measurements, it is necessary to move it in order to get rid of the interference. Moving it below the table instead of on top of it appeared to be enough to no longer cause distortions on the beam. In order to still be able to measure the temperature, since the current thermocouple cable is too short, a different thermocouple is attached to a metallic transit piece which is connected to the

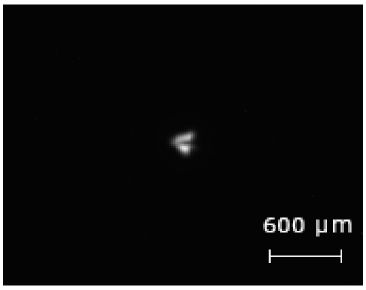

Figure 5.3: The continuous electron beam focused directly onto the detector (with the vacuum gauges on).

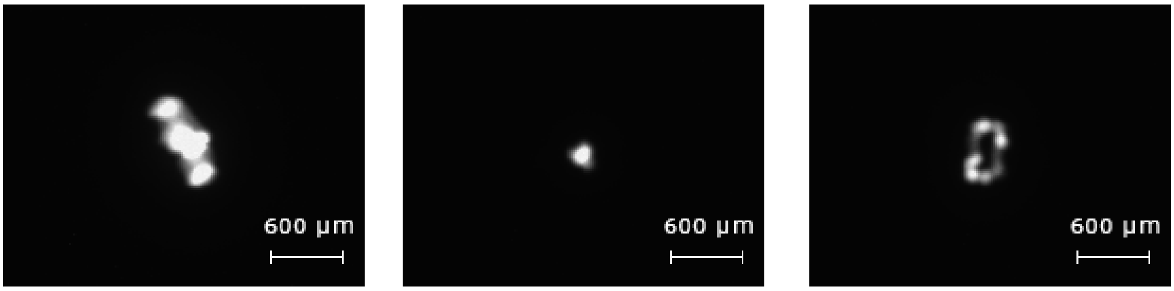

(a) (b) (c)

Figure 5.4: The continuous electron beam focused directly onto the detector with (a) the vacuum gauges plugged into different sockets, (b) the vacuum gauges turned off and (c) the water cooler turned on.

water tubes. Although measuring the temperature of the water instead of the cavity means a less stable temperature, it is still adequate.

Several other devices were found to have small but not negligible effects. One is the fan attached to the compression cavity, which is placed directly onto its PVC housing. A tube is now placed between the fan and the housing, still allowing for cooling of the cavity, yet significantly decreasing the effects of the fan on the beam. Multiple types of power supplies around the setup also emitted AC magnetic fields. By trial and error it was discovered that only the Delta Elektronika Power Supply ES 030-5 does not effect the beam, while other Delta Elektronika power supplies have a small to very small influence depending on orientation and distance. Also extra care has to be taken that no Calex BPS4000 Triple Output Power Supply is in proximity of the setup, as they are able to deform the spot from a considerable distance. In the near future, nearby setups placed in the lab should also be investigated for sources of disturbance as this has not been done yet. The pre-vacuum pump of the SEM focus column also creates a strong AC magnetic field, but it cannot be turned off for a long time. It is placed directly beneath the setup and luckily the table shields the setup from most of it, making the effects minor.

The final confirmed source of disturbance lies in the USB devices. Since the setup uses many devices, two USB hubs are used to connect them to the computer. These hubs can be powered by the computer or externally through an adapter. One of the two hubs was powered externally and this caused the entire spot to visibly oscillate on the detector, probably due to the adapter being faulty or of low quality. Powering the hub through the computer solved this issue.
The pre-amplifier and attenuators located in the splitter box in Fig. 3.6 are also powered and

controlled through one of these USB hubs. Unplugging them resulted in a position shift of the spot, meaning one or more of them probably emits a DC magnetic field.

There are also a few unconfirmed sources of disturbance, mainly around the SEM. Since the effects on the beam cannot be measured without it, turning it or parts of it off is not an option. It was found that the area around the SEM TMP was filled with AC magnetic fields at 50 Hz and 1 kHz, the latter being the rotor frequency of the pump. Magnetic fields of 30, 60 and 90 kHz were found around the electron gun, with 30 kHz the switching frequency of the high tension generator.
Finally there are some devices that are confirmed to not influence the electron beam noticeably. These are the monitor next to the setup, the bipolar current supplies, the 16W amplifiers, the VCO, the motorized stages, the beam blanker and the two TMPs attached to the beamline as well as their controllers and their power supplies.

5.2.1 Circumventing the disturbance

After the aforementioned changes were made, a waist scan was re-attempted. Although the pattern visible around the waist is still present, the changes did improve the shape of the bunches somewhat (see Fig. 5.5a compared to Fig. 5.5b). The streaking direction in these figures in different from Fig. 5.2 because the streaking cavity was rotated by approximately 90 degrees during this measurement. The streak is also slightly wider due to solenoid not focusing optimally, which in this case results in slightly more distinguishable peaks.

With the pattern becoming much more distinguishable as compared to before the discussed changes, the intensity profile of this streak along a center line was taken. This allows for approximately sixteen individual spots to be distinguished (see Fig. 5.6). These spots often seem to come in pairs, but more importantly appear to have identical FWHMs. The distinguishable peaks in the intensity profile are thus each fitted with a Gaussian with the constraint that the FWHM of each peak must be identical to the rest. The fitting procedure tries to minimize the error in the cumulative fit, which is the sum of all the individual fits. The resulting FWHM leads to a spot size $\chi = 31.3 \pm 0.2\,\mu$m, which is in agreement with the expected minimum spot size according to the GPT simulation with a similar initial pulse length. The pattern therefore is most likely the result of different bunches ending up on different discrete positions on the detector. These positions represent a certain energy and are created by a different arrival time of the electrons at the streaking cavity. As the pattern is always oriented in the streaking

(a) (b)

Figure 5.5: Compressed and streaked electron bunches on the detector with the vacuum gauges turned (a) on and (b) off. The solenoid was used to slightly defocus in the direction perpendicular to the streak in order to improve the contrast between the different peaks. The red arrow indicates the streak direction of the streaking cavity.

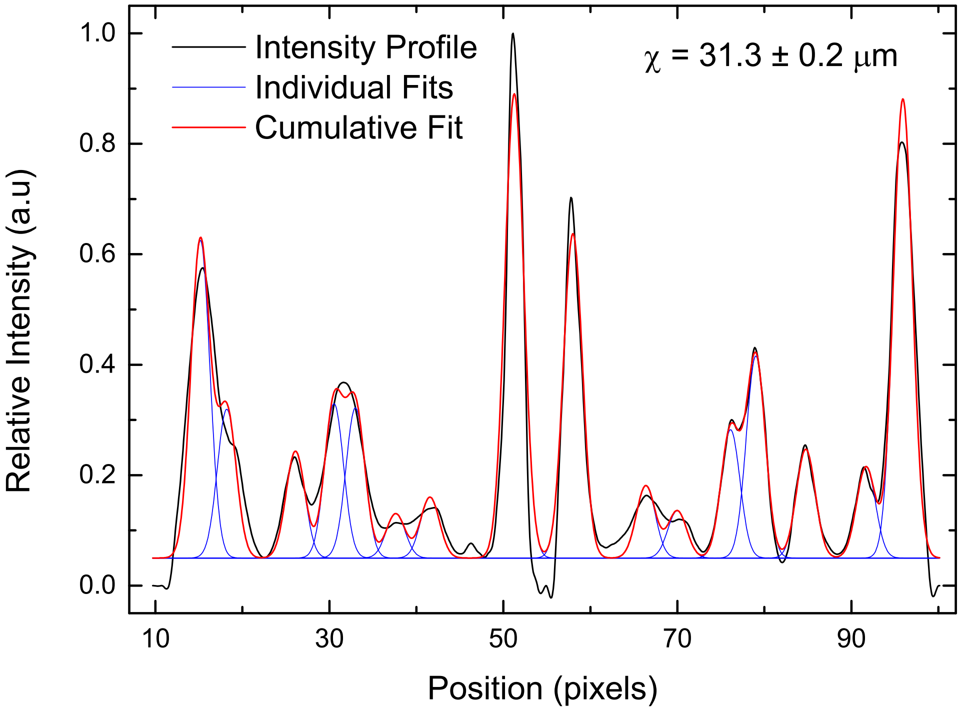

Figure 5.6: Intensity profile along a line through the middle of the streak in Fig. 5.5b. Each peak is fitted with a Gaussian with an rms width $\chi = 31.3 \pm 0.2\,\mu$m. The width of the peaks appear slightly smaller due to deconvolution methods used to clear up the image.

direction, the cause must either be a variation of the energy of the electrons by approximately 114 eV, or a difference in path length between the compression and streaking cavity creating a time difference of approximately 17 ps, measured from the first to the last peak in Fig. 5.6. The interference of the vacuum gauges, which causes the position of the peaks to change between Fig. 5.5a and Fig. 5.5b, is created by a 50 Hz signal. The cause of the pattern is therefore most likely also a 50 Hz signal.

In order to both investigate the pattern further and to circumvent it for future measurements, the beam blanker is employed. By blanking the electron bunches with a square wave with varying starting time and pulse duration at a frequency of 50 Hz synchronized to the power grid, it is possible to separate a few of the peaks in the streak. Fig. 5.7 shows the electron bunches on the detector for different pulse start times and durations, showing that one or more peaks can be lifted from the pattern. The bunches look different than before due to the alignment being different. Although this method greatly reduces the current used in a measurement, it is possible to do a proper waist scan and EELS measurement with one of these blanked pulses. Another downside is that it is difficult to see whether only one peak is lifted from the pattern or if some noise or part of another peak is lifted as well.

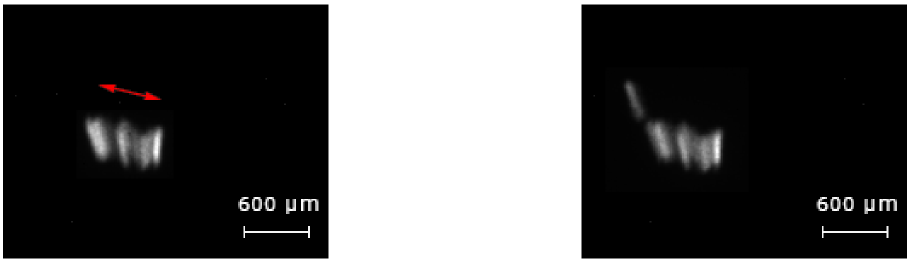

(a) No blanking

(b) Pulse start: 0 ms. Pulse duration: 2 ms.

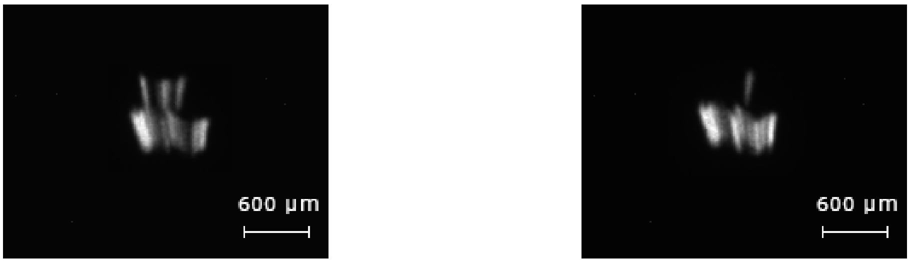

(c) Pulse start: 5 ms. Pulse duration: 5 ms.

(d) Pulse start: 9 ms. Pulse duration: 1 ms.

Figure 5.7: The compressed, streaked and partially blanked electron bunches for different starting times and duty cycles of the blanker pulse. The red arrow indicates the streak direction of the streaking cavity.

5.3 Waist scan and improved EELS

Using different amounts of power P_{chop} in the chopping cavity, the electron bunch length can be varied. With a beam blanker pulse duration of 1 ms separating one spot in the direction perpendicular to the streak direction, two waist scans were performed for different initial electron pulse lengths and their results are presented in Fig. 5.8 and Fig. 5.9. These figures show the rms spot size on the detector in the streaking direction χ_{chopped} as a function of the focal length of the compression cavity, as calculated from Eq. 5.1, and are fitted with Eq. 2.37. Fig. 5.8 also shows a GPT simulation of a waist scan. The deviation at larger focal lengths is due to the initial electron bunch lengths in the simulations being smaller than in the experiment. The insets in Fig. 5.8 and Fig. 5.9 show that around the waist the measurements are in good agreement with the theory and simulations.

Several important values can be calculated from these waist scans and are presented in Table 5.1. The minimum and uncompressed rms spot size χ_0 and χ_{min} are taken directly from the waist scans. The minimum and uncompressed pulse durations in the streaking cavity can be calculated using Eq. 4.3. At optimal compression the resulting temporal bunch length is calculated to be $\Delta t_{\text{FWHM}} = 374 \pm 2$ fs. The rms energy spread of the beam is calculated with Eq. 5.2 and found to be $\Delta E_{\text{FWHM}} = 2.59 \pm 0.03\,\text{eV}$, which is slightly higher than the 2.41 eV obtained from the simulations. The reason the simulation has a better energy resolution than the measurement even though it has a larger spot size, is due to a larger full streak length. Whereas the measurement resulted in $\chi_{\text{full}} = 19.0 \pm 0.1\,\text{mm}$, the simulation has $\chi_{\text{full}} = 22.3\,\text{mm}$ due to a larger magnetic field amplitude in the streaking cavity.

As mentioned in Section 2.3.4, the longitudinal emittance can be calculated from the waist scan and is found to be $\varepsilon_z = \sigma_E \sigma_{t_i} = (4.05 \pm 0.05) \cdot 10^{-12}\,\text{s} \cdot \text{eV}$.

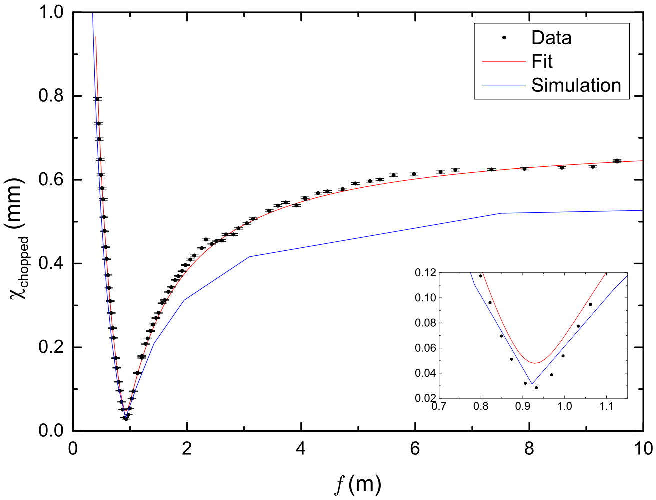

Figure 5.8: Waist scan with $P_{\text{chop}} = 2.49\,\text{W}$ forwarded power in the chopping cavity, fitted with Eq. 2.37. Smallest spot size is $28.5 \pm 0.2\,\mu\text{m}$. The blue line represents several GPT simulations with smaller initial pulse durations, resulting in $\sigma_{\text{min}} = 31.3\,\mu\text{m}$.

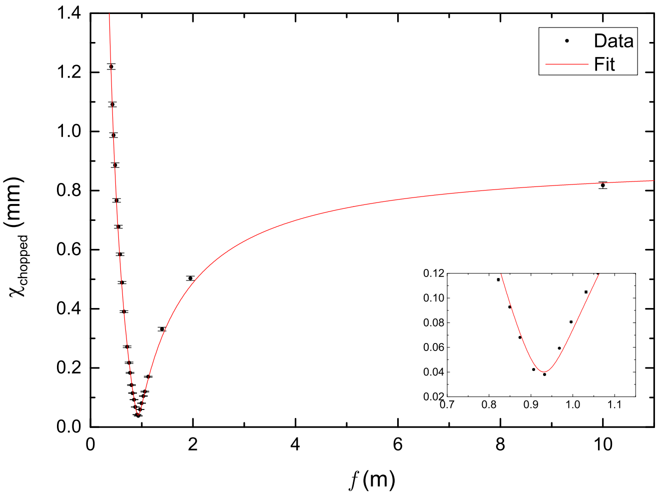

Figure 5.9: Waist scan with $P_{\text{chop}} = 1.48\,\text{W}$ forwarded power in the chopping cavity, fitted with Eq. 2.37. Smallest spot size is $38.0 \pm 0.7\,\mu\text{m}$.

Table 5.1: The waist scan results for the two powers in the chopping cavity, with respectively χ_0 and χ_{min} the uncompressed and compressed rms spot size on the detector in the streaking direction, σ_{t_0} and $\sigma_{t,\text{min}}$ the uncompressed and compressed rms pulse duration at the streaking cavity and σ_E the rms energy spread of the beam. All uncertainties in 1σ intervals.

$P_{\texttt{chop}}(\text{W})$	$\sigma_{t_0}(\text{ps})$	$\sigma_{t,\text{min}}(\text{ps})$	$\chi_0(\mu\text{m})$	$\chi_{\text{min}}(\mu\text{m})$	$\sigma_E(\text{eV})$
2.49 ± 0.01	3.72 ± 0.02	0.159 ± 0.001	660 ± 3	28.5 ± 0.2	1.10 ± 0.01
1.48 ± 0.01	4.57 ± 0.06	0.213 ± 0.004	$(82 \pm 1) \cdot 10^1$	38.0 ± 0.7	1.47 ± 0.03

With the compression cavity working as intended, five electron energy loss spectra are taken using the cross grating sample containing a polycrystalline gold layer deposited on a carbon film. Fig. 5.10 shows one of the detector images obtained from this measurement. For analysis, the counts on the detector along a line in the streaking direction are taken and normalized with the total amount of counts along that line. Averaging the five spectra, the result is plotted versus the energy loss in Fig. 5.11, with the ZLP placed at 0 eV energy loss. A measurement taken without a sample present is also shown. Fitting the zero-loss peak with a Gaussian and taking into account the uncertainty in L_2 results in an energy resolution $\Delta E_{\text{FWHM}} = 2.3 \pm 0.1$ eV. The difference with the energy resolution obtained from the waist scan is probably caused by solenoid. Since its focus on the detector is near the aberration limit, small misalignments can lead to a significant increase in spot size.
Comparing the results between the three-cavity setup and the two-cavity setup, of which the latter has an energy resolution of $\Delta E_{\text{FWHM}} = 10.8 \pm 0.2$ eV and is also shown in Fig. 5.11, the addition of a compression cavity greatly improves the energy resolution of the ToF-EELS method. The arise of a plasmon peak around approximately 20 eV energy loss due to the sample is evident when comparing the spectrum with and without the sample in Fig. 5.11, while the EELS spectrum also shows a slightly broader ZLP. This broadening is most likely due to scattering on the sample.

An important thing to note about these spectra is the behaviour outside the ZLP. For the spectrum taken without a sample present, the counts outside the zero loss peak should quickly drop to the noise level. The spectra with a sample present should also show this quick drop in the region in front of the ZLP. The spectrum without the sample present in Fig. 5.11 however shows a steady (logarithmic) drop around the ZLP, only becoming noise-dominated beyond 50 eV energy loss. When looking at the unnormalized counts (see Fig. B.1) a difference between the measurements with two-cavity setup and the three-cavity setup becomes clear: in the two-cavity setup the electron count in front of the ZLP does indeed quickly drop to the noise level, while it does not in the three-cavity setup. Looking at the detector image shown in Fig. 5.10, the unblanked, distorted electron spot partially visible in the top-right corner is surrounded by a large area of noise, which would explain this difference. Not only does this noise overlap with the blanked spot, the blanking itself carries with it some of this noise since not exactly one spot is singled out from the pattern. Getting rid of the source of the 50 Hz disturbance should solve this issue.

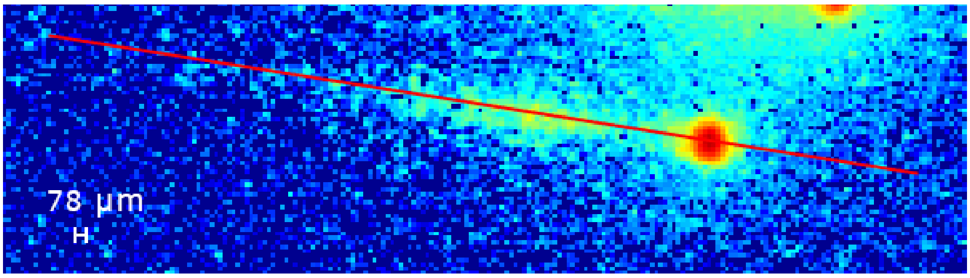

Figure 5.10: The detector image of the blanked and unblanked spot plotted on a logarithmic scale. The data along the red line is taken for analysis. False color.

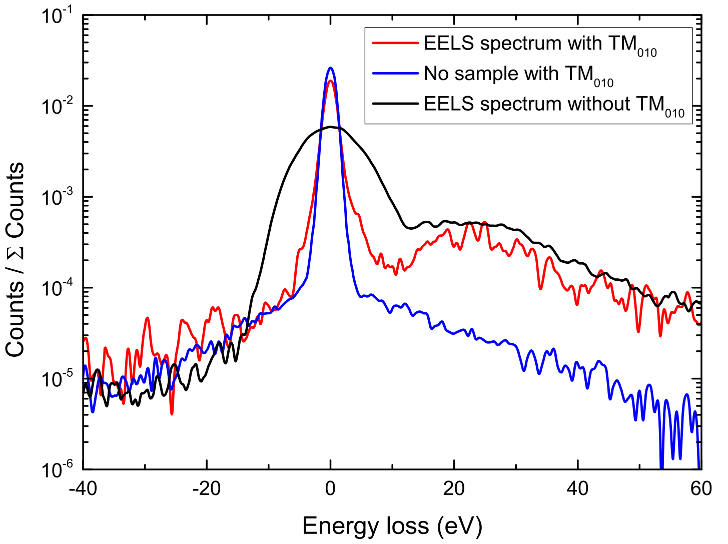

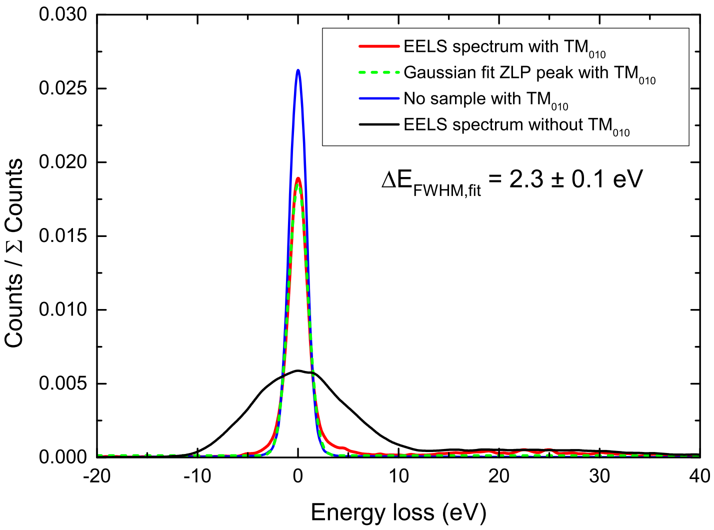

Figure 5.11: The electron energy loss spectra with and without using the compression cavity, having both a ZLP and a plasmon peak, as well as the spectrum with no sample present which only has a ZLP. The spectra are plotted logarithmically (top) and linearly (bottom). The ZLP of the electron energy loss spectrum with the compression cavity has a FWHM of 2.3 ± 0.1 eV.

Chapter 6

Conclusion & Outlook

6.1 Conclusion

In this thesis an improvement to the previously existing ToF-EELS setup was made. This was done by implementing a TM_{010} microwave cavity in order to compress the electron bunches and separate them by their energy. The goal was to show that this would improve the energy resolution of the setup. In order to confirm the current performance, a ToF-EELS measurement was performed. From this measurement it was found that the result is not the same after a 180 degrees phase shift of the electromagnetic fields in one of the two cavities. Simulations revealed that this is caused by the solenoid which is used to focus the electron bunches. When electron bunches pass through the solenoid under an angle, a z-x correlation is induced. The bunches then get streaked in the direction either opposite or parallel to this correlation, where changing the phase by 180 degrees switches between the two. This results in a slightly different deflection for the two phases. Nonetheless an energy resolution of $\Delta E_{\mathrm{FWHM}} = 10.8 \pm 0.2$ eV and an upper limit to the temporal resolution of $\Delta t_{\mathrm{FWHM}} = 2.43 \pm 0.06$ ps was obtained from these measurements.

In order to implement the new cavity several changes had to be made to the setup. Firstly the location of the compression cavity was considered. For optimal performance the distance towards the streak cavity should be maximized. This leads to a distance of approximately 0.93m between the compression and streak cavity and a distance of 0.79 m between the compression cavity and the sample. From simulations it followed that with these distances the minimum achievable spot size would be 31.3 μm with a corresponding energy resolution of 2.41 eV, where the electron bunch has an energy spread of 2.37 eV directly after exiting the slit.
The second consideration was the placement of the second streak cavity. Due to another experiment it had been removed from the setup and had to be reimplemented. There were two requirements in order to do this. One was that the length of the setup should not increase by more than 17 mm so that the electron detector does not extend beyond the table. The other was that it should be relatively easy to remove the cavity from the setup, so the other experiment could take place in parallel. In order to satisfy both these requirements, it was opted to place the streak cavity inside a CF63 cube, which is both small in size and easy to open. Several other small adjustments were made to either make alignment easier, such as additional steering coils, or to decrease material requirements, such as additional loops in the Earth magnetic field correction. Aside from the vacuum components, a new infrastructure for the control of the RF signals was created, which includes phase and power control, including software, for four distinct cavities in their respective power ranges.

With the new setup complete a waist scan using the TM_{010} cavity was performed. It was found that the electron bunch did not compress properly and that a pattern emerged around the focus. Suspecting electromagnetic interference from surrounding devices, a Faraday cup and an AC magnetic field meter were used to investigate. While the Faraday cup measured no AC effects, the AC magnetic field meter found several devices emitting relatively strong magnetic fields. By moving them away from the setup or by turning them off during a measurement the beam quality was increased. This however was not the source of the pattern around the focus. By using the beam blanker present in the setup with its signal synchronized to the power grid, it was possible to separate one or multiple of the spots from the pattern, allowing for a proper measurement and revealing that the source of electromagnetic interference causing the pattern operates at that frequency.

New waist scans were performed and a minimum spot size of $28.5 \pm 0.2\,\mu$m was found. Together with the uncompressed spot size of $660\pm3\mu$m, the longitudinal emittance of the electron bunches was calculated to be $(4.05 \pm 0.05) \cdot 10^{-12}$ s · eV, achieving a temporal spread at the streaking cavity of $\Delta t_{\mathrm{FWHM}} = 374 \pm 2$ fs and an energy resolution of $\Delta E_{\mathrm{FWHM}} = 2.59 \pm 0.03$ eV.

With the effect of the compression cavity known, a sample containing a polycrystalline gold layer deposited on a carbon film was inserted, causing a plasmon peak to arise at approximately 20 eV energy loss. Performing an EELS measurement resulted in an energy resolution of 2.3 ± 0.1 eV. Comparing this to the EELS spectrum obtained before inserting the compression cavity, an improvement of almost a factor five is realized, achieving the initial goal. Small discrepancies in energy resolutions measured in the waist scan and the EELS measurement are due to the difficulties in aligning the solenoid, which adds aberrations to the detector image.

6.2 Recommendations & Outlook

Although the addition of a TM_{010} cavity has been shown to increase the energy resolution of the ToF-EELS setup, there is still room for improvement. This section will address some unresolved issues with the setup, as well as future possibilities to go beyond the current limits.

After the realization of the new design for the setup, the electromagnetic interference causing the aforementioned pattern was a huge roadblock. Although by using the beam blanker as a workaround it is possible to perform EELS measurements, the interference still causes major issues. First is the large amount of noise around the electron spot. This is created by the electrons in the unblanked pattern, of which there are many more than in the blanked spot.
The second issue is the loss of current due to picking out one spot from the pattern. While there are still enough electrons ending up in the ZLP, the amount of electrons ending up at the plasmon peak is very little.
The third issue is the presence of the beam blanker. With the addition of the TM_{010} cavity, alignment has become increasingly difficult. Removing the beam blanker would reduce the difficulty again. It would also allow the compression cavity to be placed at a greater distance from the streak cavity. Considering these three issues, getting rid of the interference causing the pattern is vital.

Continuing with electromagnetic interference, there is also room for improvement in the stability of the beam. Although there is a coil surrounding the entire setup, the Earth magnetic field is not constant. Not only that, there are multiple experiments running in the lab, as well as many other possible sources of magnetic fields. This results in the magnetic field around our setup to change not only in time, but along the length of the setup as well. In order to stabilize the beam, an active stabilization system has to be created by measuring the magnetic field at at least one but preferably multiple positions and using them to control coils around the setup in order to compensate for external magnetic fields.

Aside from resolving the issues mentioned above, there are two ways in which the energy resolution of the setup can be increased substantially. One of those will be discussed in Section 6.2.1, the other one is by replacing the electron gun. The SEM currently in use is a rather old thermionic emitter with an energy spread of 1–3 eV. Using a field emission gun with a typical energy spread of 0.3–0.6 eV[34] and a normalized transverse emittance of up to two orders of magnitude smaller than a thermionic emitter would drastically improve both the amount of electrons hitting the detector and both the temporal and energy resolution of the system.

In addition to improving the performance, the setup may also be used for different types of research. One such way is by using a dual mode TM_{110} cavity. In such a cavity the TM_{110} mode is excited twice in perpendicular directions with a slight difference in resonant frequency. This type of cavity is being developed at CQT with a difference in resonant frequencies of 75 MHz. Doing this will streak a continuous beam not in a straight line but along a Lissajous curve. Placing an aperture behind the cavity will then create electron bunches at 75 MHz. Synchronizing these bunches with a 75MHz laser present in our lab would allow for time-resolved measurements at a high repetition rate, such as pump-probe experiments. Another possibility is the use of the remaining transverse direction. Using longitudinal optics energy is imaged in the streaking direction. The direction perpendicular to this is currently unused. Employing regular transverse optics to image diffractions, both energy and momentum information can be obtained simultaneously, allowing for the measurement of dispersion curves.

6.2.1 A fourth cavity

In this project a TM_{010} cavity has been used to focus the electron bunches longitudinally. An important restriction to the achievable pulse lengths is the initial energy spread of the beam. In order to reduce this energy spread, expensive and complex monochromators are often used. A fourth cavity presents a different and cheaper method of monochromation. Because phase space density must be conserved, increasing the pulse length will lead to a decrease in uncorrelated energy spread. Thus by increasing the pulse length of the electron bunches just before they pass through the sample, smaller energy losses can be separated. This can be done with a TM_{010} cavity, where a π phase shift causes the behaviour of the cavity to switch from compression to stretching. A longitudinal phase space representation of this four-cavity method is shown in Fig. 6.1. Here an electron bunch with an initial energy spread is first defocused by a TM_{010} cavity, after which a drift space allows the bunch to stretch in time. The stretched bunch then interacts with a sample, inducing energy losses. A TM_{010} cavity is again used to compresses the bunch in order to separate the different energies. However, this method does come at a cost of temporal resolution due to the stretching. Alternatively, the first TM_{010} cavity can also be used to gain temporal resolution at a cost of energy resolution.

Some initial simulations have been performed on this four-cavity method. Starting with a 90 fs electron bunch created by the chopping cavity, it is stretched with a TM_{010} cavity to 3 ps at the sample where energy losses of 0, 60, 120 and 180 meV are added. The compression cavity then separates the energies and the streaking cavity places them on the detector. Fig. 6.2(a) shows the longitudinal phase space in the center of the deactivated streaking cavity. Although aberrations are present, they are not dominant. In Fig. 6.2(b) the detector image acquired from this simulation is shown, from which an energy resolution of 24 meV is obtained, which is almost a factor hundred less than the 2.3 eV obtained from the three-cavity setup.

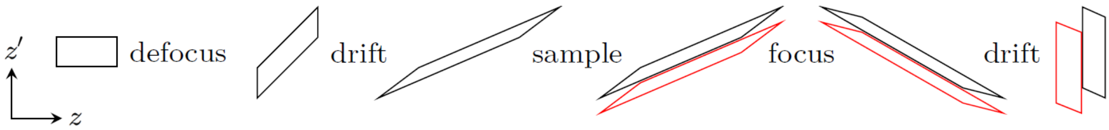

Figure 6.1: Phase space representation of four-cavity EELS from the slit to the streaking cavity. An electron bunch with an initial energy distribution are first stretched. A drift space later the bunch interacts with a sample, causing some electrons to lose energy as indicated in red. The compression cavity then focuses the electron bunch to achieve energy separation. *From* [35].

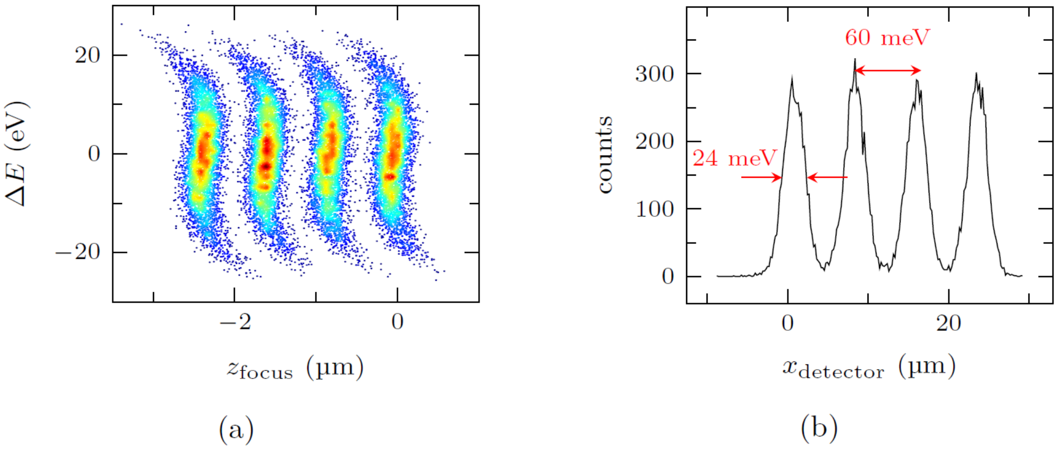

Figure 6.2: Simulation on a four-cavity setup where four distinct energy losses are added to the electrons. (a) The longitudinal phase space in the center of the streaking cavity when it is turned off. (b) Transverse positions on the detector, showing clear separation of each energy loss peak with an energy resolution of 24 meV. *From* [35].

Bibliography

[1] Ruska E. (1986). Ernst Ruska Nobel Prize Autobiography. `http://www.nobelprize.org/nobel_prizes/physics/laureates/1986/ruska-bio.html`. Accessed: 2016-10-10. ↑

[2] Scherzer O. (1936). Über einige Fehler von Elektronenlinsen. *Zeitschrift für Physik*, vol. 101(9):pp. 593–603. ↑

[3] Hawkes P.W. (2009). Aberration correction past and present. *Philosophical Transactions of the Royal Society of London A: Mathematical, Physical and Engineering Sciences*, vol. 367(1903):pp. 3637–3664. ↑

[4] Zach J. (1990). Resolution limits in low voltage scanning electron microscopes using retarding objective lenses. *Nuclear Instruments and Methods in Physics Research Section A: Accelerators, Spectrometers, Detectors and Associated Equipment*, vol. 298(1):pp. 255–259. ↑

[5] Zach J. & Haider M. (1995). Aberration correction in a low voltage SEM by a multipole corrector. *Nuclear Instruments and Methods in Physics Research Section A: Accelerators, Spectrometers, Detectors and Associated Equipment*, vol. 363(1):pp. 316–325. ↑

[6] Krivanek O. et al. (1997). Aberration correction in the STEM. In *Electron Microscopy and Analysis*, 153, pp. 35–39. Institute of Physics, Bristol, UK. ↑

[7] Haider M. et al. (1998). Electron microscopy image enhanced. *Nature*, vol. 392(6678):pp. 768–769. ↑

[8] Uhlemann S. & Haider M. (1998). Residual wave aberrations in the first spherical aberration corrected transmission electron microscope. *Ultramicroscopy*, vol. 72(3–4):pp. 109–119. ↑

[9] Batson P.E., Dellby N., & Krivanek O.L. (2002). Sub-ångstrom resolution using aberration corrected electron optics. *Nature*, vol. 418(6898):pp. 617–620. ↑

[10] Hawkes P.W. & Spence J.C.H. (2007). *Science of Microscopy*. Springer Science+Business Media, LLC, New York NY. ↑

[11] Sciaini G. & Miller R.J.D. (2011). Femtosecond electron diffraction: heralding the era of atomically resolved dynamics. *Reports on Progress in Physics*, vol. 74(9):p. 096101. ↑

[12] Flannigan D., Lobastov V., & Zewail A. (2007). Controlled Nanoscale Mechanical Phenomena Discovered with Ultrafast Electron Microscopy. *Angewandte Chemie International Edition*, vol. 46(48):pp. 9206–9210. ↑

[13] Shorokhov D. & Zewail A.H. (2016). Perspective: 4D ultrafast electron microscopy - Evolutions and revolutions. *The Journal of Chemical Physics*, vol. 144(8):080901. ↑

[14] Egerton R.F. (2011). *Electron Energy-Loss Spectroscopy in the Electron Microscope.* Springer Science+Business Media, LLC, Boston MA, 3rd ed. ↑, ↑, ↑

[15] Bellido E. et al. (2016). Very High Resolution Energy Loss Spectroscopy: Applications in Plasmonics. *Microscopy and Microanalysis*, vol. 22(S3):pp. 974–975. ↑

[16] Grogger W. et al. (2008). An Introduction to High-resolution EELS in Transmission Electron Microscopy. *Topics in Catalysis*, vol. 50(1):pp. 200–207. ↑

[17] Van Ninhuijs M. (2016). *Time-of-Flight Electron Energy Loss Spectroscopy by using miniaturized RF technology* (Master thesis). Eindhoven University of Technology. ↑, ↑, ↑

[18] Mancini G. et al. (2012). Design and implementation of a flexible beamline for fs electron diffraction experiments. *Nuclear Instruments and Methods in Physics Research. Section A: Accelerators, Spectrometers, Detectors and Associated Equipment*, vol. 691:pp. 113–122. ↑

[19] van Oudheusden T. et al. (2010). Compression of Subrelativistic Space-Charge-Dominated Electron Bunches for Single-Shot Femtosecond Electron Diffraction. *Phys. Rev. Lett.*, vol. 105:p. 264801. ↑

[20] Pasmans P. et al. (2013). Microwave TM010 cavities as versatile 4D electron optical elements. *Ultramicroscopy*, vol. 127:pp. 19 – 24. ↑

[21] Pozar D.M. (2011). *Microwave Engineering.* Wiley, Chichester, 4th ed. ↑

[22] Lassise A. (2012). *Miniaturized RF technology for femtosecond electron microscopy* (Doctoral dissertation). Eindhoven University of Technology. `http://repository.tue.nl/739203`. ↑, ↑

[23] Van Oudheusden T. (2010). *Electron source for sub-relativistic single-shot femtosecond diffraction* (Doctoral dissertation). Eindhoven University of Technology. `http://repository.tue.nl/693519`. ↑, ↑, ↑, ↑

[24] Handbook of Chemistry and Physics. `http://hbcponline.com`. Accessed: 2017-03-13. ↑

[25] Van Oostrom M. (2017). *karakterisering van een dual-mode RF cavity voor ultrasnelle elektronen microscopie* (Bachelor thesis)(Dutch). Eindhoven University of Technology. ↑

[26] Pasmans P. (2014). *Ultrafast electron diffraction: an investigation of fundamental limits* (Doctoral dissertation). Eindhoven University of Technology. `http://repository.tue.nl/774388`. ↑, ↑

[27] Wiedemann H. (2015). *Particle Accelerator Physics.* Springer International Publishing, Cham, 4th 2015. ed. ↑

[28] Franssen J. (2015). *Longitudinal phase space characterization of ultra-cold electron bunches* (Master thesis). Eindhoven University of Technology. ↑

[29] Egerton R.F. (2009). Electron energy-loss spectroscopy in the TEM. *Reports on Progress in Physics*, vol. 72(1):p. 016502. ↑, ↑

[30] See www.tvips.com for more information on the detector. ↑

[31] Verhoeven W. et al. (2016). Time-of-flight electron energy loss spectroscopy using TM110 deflection cavities. *Structural Dynamics*, vol. 3(5):p. 054303. ↑, ↑

[32] See http://www.agarscientific.com for more information. ↑

[33] See http://www.pulsar.nl/gpt for more information on the software. ↑

[34] Reimer L. & Kohl H. (2008). *Transmission electron microscopy: physics of image formation*, vol. 36. Springer, New York, NY, 5th ed. ↑

[35] Verhoeven W. (2017). *Time-Resolved EELS Using Longitudinal Optics* (Report). Eindhoven University of Technology, Department of Physics. ↑

Appendix A

Dimensions of the TM_{010} and TM_{110} cavity

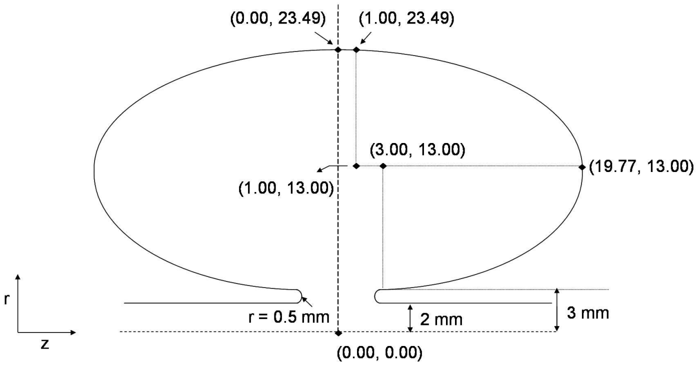

Figure A.1: Cross-section of the TM_{010} cavity. All dimensions are in (z, r) coordinates in mm with the cavity cylindrically symmetric around the z-axis. *From* [23].

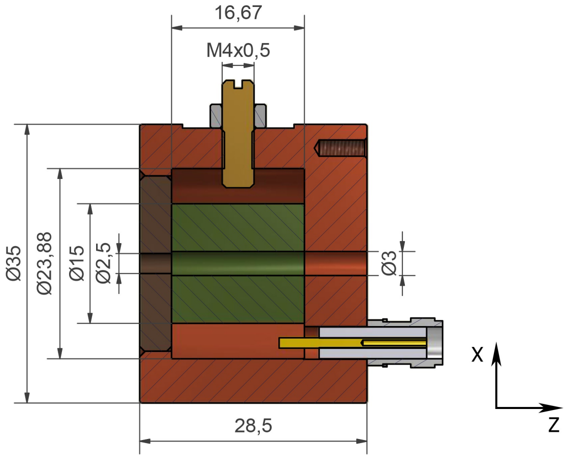

Figure A.2: Cross-section of the TM_{110} cavity. The z-axis runs through the electron hole. All dimensions are in mm.

Appendix B

Unnormalized EELS spectra

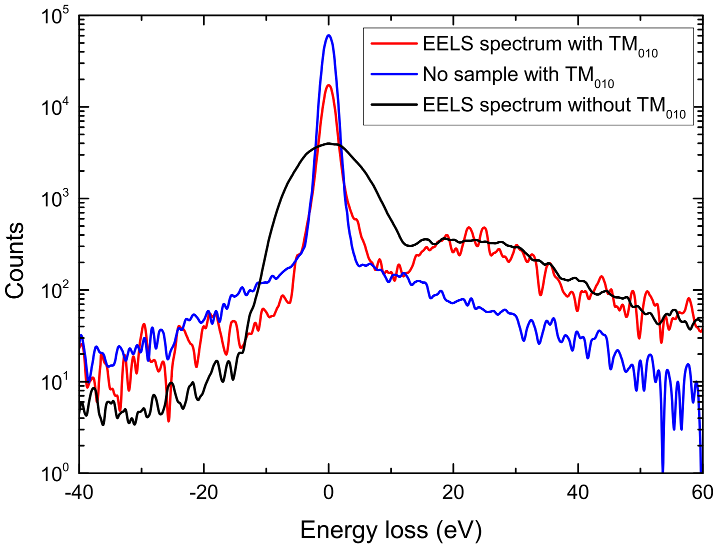

Figure B.1: The electron energy loss spectra for the two-cavity and three-cavity setup, as well as a spectrum with no sample present. Plotted on the vertical axis is the electron count on the detector.